Highlights

Scene-based spectral characterization of spaceborne imaging spectrometers in different spectral windows

Zhipeng Pei, Ge Han*, Javier Roger, Wei Gong, Luis Guanter

- Scene-based spectral calibration without reliance on onboard calibration hardware.
- Spectral shifts and channel broadening are retrieved from at-sensor radiance.
- Spectral miscalibration leads to up to 37% underestimation of methane emissions.

Scene-based spectral characterization of spaceborne imaging spectrometers in different spectral windows

Zhipeng Pei[a,c], Ge Han*[a], Javier Roger[b], Wei Gong[c], Luis Guanter[b]

[a]*School of Remote Sensing and Information Engineering, Wuhan University, Wuhan, China*
[b]*Research Institute of Water and Environmental Engineering (IIAMA), Universitat Politecnica de Valencia, Valencia, Spain*
[c]*State Key Laboratory of Information Engineering in Surveying, Mapping and Remote Sensing, Wuhan University, Wuhan, China*

Abstract

Accurate knowledge of the spectral response of spaceborne imaging spectrometers, including center wavelength (CW) and full width at half maximum (FWHM), is essential for reliable retrievals of atmospheric and surface parameters from at-sensor radiance data. Pre-flight characterizations often fail to capture changes in spectral response arising from launch, orbital conditions, and instrument aging, necessitating in-flight characterization. In this contribution, we develop a scene-based spectral calibration algorithm that operates on at-sensor radiance fitting, incorporating rigorous atmospheric radiative transfer modeling to account for coupling between gaseous absorption and atmospheric scattering effects. The algorithm models surface reflectance using polynomials and simultaneously retrieve CW and FWHM shifts across the instrument swath. Sensitivity analysis investigates the potential impacts of various factors on the calibration algorithm, revealing that water vapor uncertainty significantly affects calibration accuracy, with 5 mm uncertainty causing bandwidth errors up to 0.75 nm in a specific window. Surface reflectance characteristics also influence performance, with spectrally non-linear surfaces introducing systematic biases. We applied the method to four spaceborne imaging spectrometers: EnMAP, PRISMA, GF-5A AHSI, and EMIT, revealing distinct performance characteristics and temporal evolution patterns. EnMAP demonstrates stable spectral performance with systematic spectral shifts below 0.4 nm and peak-to-peak (P2P) differences under 1 nm in both VNIR and SWIR regions. GF-5A AHSI exhibits excellent across-track uniformity in VNIR (P2P difference in CW <0.1 nm) and shows segmented variations in SWIR due to its spectial design. PRISMA displays significant temporal degradation with P2P differences reaching 3.8 nm and 6.15 nm for CW and FWHM, respectively. EMIT shows characteristic m-shaped patterns with moderate across-track variability. Quantitative assessment reveals that spectral miscalibration can cause up to 37% systematic underestimation in methane emission quantification. The proposed algorithm provides a cost-effective complement to on-board calibration systems, enabling continuous monitoring of spectral performance and reducing potential biases in subsequent quantitative retrievals.

*Corresponding author
Email address: `udhan@whu.edu.cn` (Ge Han*)

Keywords: imaging spectrometer, spectral calibration, pushbroom

1. Introduction

Imaging spectroscopy, also known as hyperspectral imaging, emerged in the 1980s as a transformative technique that combines the spatial characteristics of traditional imaging with the detailed spectral information (Goetz et al., 1985; Goetz, 2009). The at-sensor radiance is subject to absorption and scattering caused by both the atmosphere and the surface. By acquiring contiguous narrow-band spectra for each image pixel, imaging spectrometers have been widely applied to Earth observation, including the characterization of surface composition (Carmon et al., 2020), the monitoring of vegetation physiological status (Kokaly et al., 2009), mineral mapping (Asadzadeh et al., 2024), and gas detection (Bradley et al., 2011). Of particular interest are spectrometers covering the visible to near-infrared (VNIR, ∼400–1000 nm) and shortwave-infrared (SWIR, ∼1000–2500 nm) spectral ranges with spectral resolutions between 5 and 20 nm (Ayasse et al., 2019). Early developments in imaging spectroscopy primarily relied on airborne platforms, notably the AVIRIS (please see the list of instrument abbreviations in the supplementary materials Table S1) project, which demonstrated the scientific potential of high-fidelity spectral measurements (Green et al., 1998; Thorpe et al., 2016; Green et al., 2022). Hyperion onboard EO-1 was the first spaceborne imaging spectrometer capable of collecting global hyperspectral observations, validating the feasibility of orbital hyperspectral measurements for global-scale compositional and biophysical analyses (Folkman et al., 2001). Hyperion's relatively low signal-to-noise ratio (SNR), limited spatial coverage, and spatially non-uniform detector response, highlighted the need for improved instrument designs capable of supporting robust quantitative retrievals (Pahlevan and Schott, 2013; Thompson et al., 2016). Over the past decade, satellites equipped with visible and shortwave infrared (VSWIR) imaging spectrometers have grown considerably, including GF-5 AHSI (Yinnian et al., 2020a), ZY-1 AHSI (Niu et al., 2021), PRISMA (Cogliati et al., 2021), HISUI (Yamamoto et al., 2022), EnMAP (Guanter et al., 2015; Storch et al., 2023; Chabrillat et al., 2024) and EMIT (Thompson et al., 2024). These new-generation instruments have advanced capabilities in radiometric and spectral performance, enabling more precise data processing and interpretation. To accommodate the limited integration time, orbital platforms typically employ pushbroom sensors instead of whiskbroom designs, though the former are prone to spatial uniformity in the across-track direction and spectral crosstalk between adjacent pixels (Mouroulis et al., 2000).

As measured radiance is affected by gaseous absorption, VSWIR imaging spectrometers have been proven capable of detecting trace gas plume, including nitrogen dioxide (NO_2; Borger et al. 2025), carbon dioxide (CO_2; e.g., Thorpe et al. 2023), and especially methane (CH_4; e.g., Irakulis-Loitxate et al. 2021). With improvements in hardware design and retrieval algorithm, trace gas detection has gradually evolved from qualitative detection (Roberts et al., 2010; Thompson et al., 2016) to quantitative research (Duren et al., 2019; Cusworth et al., 2024). Accurate knowledge of the spectral response of an imaging spectrometer is essential for reliable data exploitation. In most cases, a Gaussian shape is used to approximate the spectral response function (SRF), with the center wavelength (CW) and full width at half maximum (FWHM, equivalent to bandwidth) defining the channel position and the effective spectral resolution, respectively (Chrien et al., 1990; Guanter et al., 2007; Thompson et al., 2018a). Spectral calibration accuracy of $\sim$0.1 FWHM for both CW and FWHM is required to eliminate spectrally distinct errors (Green et al., 1998). Although modern instrument designs attempt to minimize systematic errors, such as defective detector elements, spatial misregistration, or optical aberrations, residual nonuniformities often persist and require dedicated calibration and correction strategies (Guanter et al., 2009b). For instance, slight shifts and rotations of the focal plane array relative to the spectrometer, as well as misalignments between the instrument slit and the detector array, can lead to linear or nonlinear spectral shift in the across-track direction. The phenomenon in which the CW of pixels near the center of the array differ slightly from those near the edges is commonly referred to as the "smile" or "frown" effect (Mouroulis et al., 2000; Gao et al., 2004). In addition, instrument defocus typically results in channel broadening, thereby altering the shape of SRF and usually manifesting as an increase in FWHM (Guanter et al., 2009b).

Although pre-flight laboratory characterization provides nominal spectral calibration parameters, the spectral behavior of instruments often changes during launch and on-orbit operations due to misalignment caused by mechanical vibrations, aging of optical or electronic components, and variations in temperature and pressure (Guanter et al., 2006). Consequently, in-flight or on-orbit spectral calibration is indispensable to track the instrument spectral performance over time and to detect potential deviations from the nominal characterization. Over the past few decades, several methods have been developed to perform in-flight spectral characterization. Some of these methods can only reliably calibrate CW, while others attempt to calibrate both CW and FWHM simultaneously. In general, these methods utilize doped spectral spheres (Baur et al., 2023), spectral filters (Coppo et al., 2020), solar Fraunhofer lines (Kuhlmann et al., 2016), or atmospheric absorption lines (Gao et al., 2004) to generate radiance with distinct and observable spectral features. The former two typically rely on artificial light sources, while the latter two depend on Earth-reflected radiation and are therefore referred to as scene-based calibration. Scene-based methods have been widely adopted due to its low hardware requirements and cost-effectiveness, making it an important complementary and validation approach. Fig.1 shows the absorption effects of individual gases on radiance spectra, with several available spectral calibration windows (A-E) marked.

In this work, we begin by reviewing previous algorithms for scene-based spectral calibration of imaging spectrometers with a spectral resolution on the order of 10 nm, and subsequently propose a new algorithm based on fitting at-sensor radiance to characterize trends in spectral shift and channel broadening in the across-track direction. This algorithm can serve as a spectral uniformity check prior to gas retrieval and can improve retrieval accuracy by updating calibration coefficients. Our objectives are to (i) introduce the algorithm and its application to spaceborne imaging spectrometers, (ii) conduct sensitivity analysis to evaluate the algorithm's response to uncertainties in atmospheric and surface parameters, (iii) analyze the sensitivity of gas retrieval to spectral shifts and channel broadening, (iv) reveal spectral uniformity and degradation in the spectral response of several representative instruments.

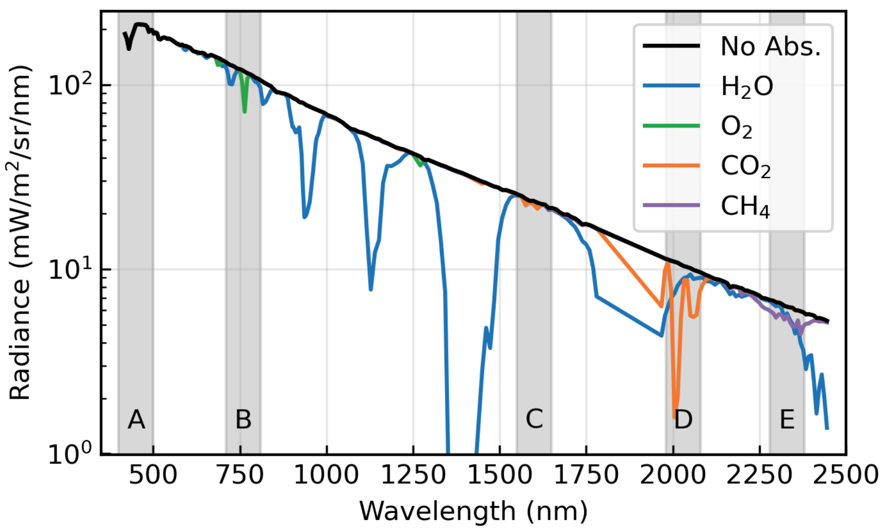

Figure 1: The simulated top-of-atmosphere (TOA) radiance spectra include cases without gas absorption (black line) and cases with individual gas absorption (colored lines). The four colored lines represent water vapor (H_2O), oxygen (O_2), carbon dioxide (CO_2), and methane (CH_4), respectively. The high-resolution spectra are generated using libRadtran with gas column amounts of 20 mm for H_2O, 20.9% for O_2, 400 ppm for CO_2, and 1.9 ppm for CH_4, assuming nadir viewing geometry (solar zenith angle = viewing zenith angle = 0°), and then convolved with a Gaussian-shaped SRF parameterized by the CW and FWHM of the EnMAP satellite. The gray-shaded areas indicate five spectral windows (A–E) suitable for calibration, specifically 400–500 nm, 710–810 nm, 1550–1650 nm, 1980–2080 nm, and 2280–2380 nm. Window A includes solar Fraunhofer lines, whereas windows B–E encompass atmospheric absorption features.

2. Methodology

2.1. Spectral Calibration Algorithm

The algorithm based on spectrum-matching techniques proposed by Gao et al. (2004) forms the basis of scene-based spectral calibration approaches for imaging spectrometers. Since this algorithm only refines CW without addressing FWHM, the simplification of neglecting atmospheric scattering effects is valid. This is because CW calibration relies on the position of absorption features, which remains unaffected by scattering, whereas FWHM calibration depends on absorption depth, which is influenced by scattering as it alters the effective photon path length. To better account for the coupling effects between gaseous absorption and atmospheric scattering, Guanter et al. (2009b) proposed a practical 2-D optimization scheme to estimate CW and FHWM simultaneously leading to the smoothest surface reflectance for high spectral resolution imaging spectrometers. This algorithm is based on the fact that surface reflectance after atmospheric correction is expected to be smooth around atmospheric absorption features. The occurrence of spikes and dips generally indicates spectral shifts or channel broadening, assuming that gas concentrations are accurately estimated. In terms of a Lambertian target, at-sensor spectral radiance $L_{\rm toa}$ is defined as (Guanter et al., 2009b)

$$L_{\rm toa} = L_{\rm p}^0 + \frac{1}{\pi}\frac{\rho E_{\rm g}^0 T_{\uparrow}}{1 - s\rho}, \tag{1}$$

where ρ is the surface reflectance, L_{p}^{0} is the intrinsic atmospheric path radiance with $\rho = 0$, E_{g}^{0} is the global irradiance flux reaching the surface with $\rho = 0$, $T_{\uparrow}$ is the total atmospheric transmittance (diffuse plus direct) in the observation direction, and s is the atmospheric spherical albedo accounting for multiple scattering between atmosphere and surface. All terms depend on wavelength λ (omitted here for clarity). Since the atmospheric parameters $\{L_{\mathrm{p}}^{0}, E_{\mathrm{g}}^{0}, T_{\uparrow}, s\}$ are independent from ρ, ρ can be obtained by analytical inversion

$$\rho = \frac{\pi \left(L_{\mathrm{toa}} - L_{\mathrm{p}}^{0}\right)}{E_{\mathrm{g}}^{0}\, T_{\uparrow} + \pi s \left(L_{\mathrm{toa}} - L_{\mathrm{p}}^{0}\right)}. \tag{2}$$

Atmospheric parameters can be calculated directly or indirectly through atmospheric radiative transfer models(e.g., MODTRAN or libRadtran) for a given observation geometry angle and atmospheric condition (Guanter et al., 2009a). By minimizing the sum of squared residuals between the surface reflectance ρ and the smoothed reflectance ρ_{sm} obtained from low-pass filtering, spectral shifts and channel broadening can be determined. A full description of this procedure can be found in Guanter et al. (2009b). Since the measurement of the imaging spectrometer can be regarded as the result of convolving the high-resolution upwelling spectral radiance with the SRF of each channel, atmospheric parameters in Eq.(2) need to be convolved first. However, the convolution of a product of two spectra does not mathematically equal the product of their individual convolutions, except when the instrument response function is infinitesimally narrow or or at least one of the spectra is not affected by the convolution (see Text S1 and Fig. S1).

To address the above issues, we propose a spectral calibration algorithm in this work that operates on at-sensor radiance rather than surface reflectance. Specifically, the atmospheric parameters $\{L_{\mathrm{p}}^{0}, E_{\mathrm{g}}^{0}, T_{\uparrow}, s\}$ are computed using libRadtran based on the geometric angles and atmospheric conditions of the observed scene. The surface reflectance ρ is modeled as (Ayasse et al., 2023):

$$\rho = \sum_{d=0}^{2} \alpha_d P_d(\lambda) \tag{3}$$

where $P_d(\lambda)$ is a Legendre polynomial of degree d, and α_d is the corresponding coefficient. The wavelength range within the calibration window needs to be normalized to span from -1 to 1.

The high-resolution L_{toa} is then obtained using Eq.(1). For each spectral channel i, the convolved radiance L_i is calculated by integrating the product of the SRF (serving as a weighting function) and L_{toa} over the spectral range (Green et al., 1998).

$$L_i = \int \mathrm{SRF}_i(\lambda)\, L_{\mathrm{toa}}(\lambda)\, \mathrm{d}\lambda. \tag{4}$$

When a spectral shift δ_1 and channel broadening δ_2 are present, the Gaussian-shaped SRF of channel i is given by (Guanter et al., 2009b):

$$\mathrm{SRF}_i\big(\lambda;\, \delta_1,\, \delta_2\big) = \exp\left[-\left(\frac{\lambda - \left(\lambda_{c,i} + \delta_1\right)}{C\left(f_i + \delta_2\right)}\right)^2\right], \tag{5}$$

where $\lambda_{c,i}$ and f_i are the nominal CW and FWHM of channel i, respectively, and $C = (4\ln 2)^{-\frac{1}{2}}$. In summary, the Merit Function χ^2 to be minimised is

$$\chi^2(\delta_1, \delta_2, \alpha_0, \alpha_1, \alpha_2) = \sum_{i=1}^{\mathrm{NB}} \left[L_i(\delta_1, \delta_2, \alpha_0, \alpha_1, \alpha_2) - L_i^{\mathrm{obs}} \right]^2, \tag{6}$$

where NB is the number of spectral bands within the calibration window, and L_i^{obs} is the observed radiance in channel i. Here we employ the Nelder-Mead nonlinear least-squares optimization for spectrum-matching (Nelder and Mead, 1965). Furthermore, some studies use exhaustive grid search over predefined parameter ranges to perform the aforementioned minimization (Gao et al., 2004; Guanter et al., 2006; Yamamoto et al., 2022).

In addition, the 1-σ uncertainties of the retrieved parameters are estimated using standard errors derived from the covariance matrix of the nonlinear least-squares optimization. Following the approach described by Press et al. (2007), the covariance matrix is computed as:

$$\mathbf{C} = \sigma^2(\mathbf{J}^T\mathbf{J})^{-1}, \tag{7}$$

where $\mathbf{J}$ is the Jacobian matrix of partial derivatives of the forward model with respect to the state vector (δ_1, δ_2, α_0, α_1, α_2) parameters, and σ^2 is the residual variance estimated from the optimized fit:

$$\sigma^2 = \frac{\sum_{i=1}^{\mathrm{NB}}(L_i - L_i^{\mathrm{obs}})^2}{N_{\mathrm{dof}}}, \tag{8}$$

where $N_{\mathrm{dof}} = \mathrm{NB} - N_{\mathrm{param}}$ is the degrees of freedom, with $N_{\mathrm{param}} = 5$ representing the number of parameters in the state vector. The Jacobian matrix is computed numerically using finite differences. The standard errors of each parameter, σ_{param}, are then obtained as the square root of the diagonal elements of the covariance matrix: $\sigma_{\mathrm{param}} = \sqrt{\mathrm{diag}(\mathbf{C})}$.

The calibration uncertainties are primarily governed by three factors: (i) measurement noise in the observed radiance spectra, which directly contributes to the residual variance σ^2; (ii) forward model errors arising from approximations in atmospheric radiative transfer calculations and surface reflectance parameterization; and (iii) the sensitivity of observed radiance to spectral parameters, as characterized by the magnitude of the Jacobian matrix elements. Higher spectral sensitivity (i.e., larger Jacobian values) generally leads to reduced parameter uncertainties, which explains why spectral windows characterized by strong atmospheric absorption features tend to yield more robust calibration results than windows dominated by continuum radiance.

For practical calibration, observation scenes should preferably be selected over homogeneous surfaces in areas with minimal human activity, where atmospheric gas concentrations (except water vapor) remain relatively stable over short timescales. Water vapor exhibits widespread and strong absorption features across the 400-2500 nm range (see Fig.1), with typical column concentrations ranging from 0.6 to 4.3 cm (Gao et al., 1993). We used the three-channel ratioing technique to retrieve columnar water vapor, representing the integrated water vapor amount from ground to space (Gao and Kaufman, 2003). The retrieved values were validated using the mean columnar water vapor from the EnMAP L1 product with abundant auxiliary information (see Fig.S2 in supplementary materials for details). The CO_2 column concentration (XCO_2) and CH_4 column concentration (XCH_4) are obtained from the nearest spatiotemporal observations of OCO-2 and TROPOMI data products, respectively. While these values may not perfectly represent the actual concentrations within the scene, they represent the best available approximation given the current data sources. The impact of absorbing-gas concentration uncertainties on spectral calibration will be discussed in the following section.

The spectral radiance in the along-track direction are acquired by the same detector element through push-broom scanning. Therefore, the spectral response of pixels along this direction should be consistent. The processing begins by averaging spectra from all pixels in the along-track direction to improve the SNR and to ensure a representative sampling of the sensor's cross-track response. Even highly homogeneous desert surfaces exhibit notable topographic variations when observed at spatial resolutions of tens of meters (see Fig.S3). Thus, spectral averaging also serves to minimize terrain-induced variability (Cosnefroy et al., 1996). To avoid biases caused by surface heterogeneity, pixels within the scan swath that exhibit significant spectral differences (e.g., cloud and water areas) are excluded from the analysis. This step yields a set of averaged spectra L^{obs}, which reliably capture the spectral characteristics of the instrument and serve as input spectra for further calibration.

2.2. Radiative Transfer Model

Accurate modeling of solar radiation interactions with the Earth system (surface and atmosphere) is crucial for spectral calibration. libRadtran is one of the most widely used radiative transfer models due to its open-source availability and high flexibility (Emde et al., 2016). By default, libRadtran employs the Representative Wavelength Absorption Parameterization (REPTRAN) band parameterization to represent gaseous absorption (Gasteiger et al., 2014), which is able to generate radiance/irradiance with spectral resolution up to 0.1 cm^{-1}. Combined with its rigorous coupling of absorption and scattering, it's a good tool for simulating multi- or hyperspectral datasets.

Among the atmospheric parameters in Eq.(2), the term E_{g}^{0} can be directly given by libRadtran as standard output, while the others need to be calculated via algebraic operations as follows (Guanter et al., 2009a):

$$s = \frac{E_{\mathrm{g}}^{\rho_2} - E_{\mathrm{g}}^{\rho_1}}{\rho_2 E_{\mathrm{g}}^{\rho_2} - \rho_1 E_{\mathrm{g}}^{\rho_1}}, \tag{9}$$

$$T_{\uparrow} = \frac{\pi (L_{\mathrm{toa}}^{\rho_2} - L_{\mathrm{toa}}^{\rho_1})}{E_{\mathrm{g}}^{0}\left(\frac{\rho_2}{1-s\rho_2} - \frac{\rho_1}{1-s\rho_1}\right)}, \tag{10}$$

$$L_{\mathrm{p}}^{0} = L_{\mathrm{toa}}^{\rho_3} - \frac{T_{\uparrow} E_{\mathrm{g}}^{\rho_3} \rho_3}{\pi}, \tag{11}$$

where $E_{\mathrm{g}}^{\rho_1}$ and $L_{\mathrm{toa}}^{\rho_1}$ denote the global irradiance flux and top-of-atmosphere radiance when the surface reflectance is ρ_1, respectively, with similar notation for other subscripts.

2.3. Instrument and study sites description

The proposed spectral calibration algorithm has been applied to several widely used spaceborne imaging spectrometers, including EnMAP, PRISMA, GF-5 AHSI, and EMIT. A summary of these instrument specifications is shown in Table 1, and the detailed calibration results are presented in the Section 4.

Table 1: Specifications of EnMAP, PRISMA, GF-5 AHSI, and EMIT spaceborne imaging spectrometers. EnMAP, PRISMA, and GF-5 AHSI are dual-spectrometer designs, therefore their spectral sampling and spectral resolution show the average values for VNIR and SWIR respectively, while EMIT adopts a single spectrometer design, thus its spectral sampling and spectral resolution show the average values across the entire spectral measurement range. Note that these values are statistically obtained from measured data, and slight variations may exist for data acquired at different times.

	EnMAP	PRISMA	GF-5 AHSI	EMIT
Dispersive element	prism	prism	grating	grating
Spectral range	420-2450 nm	400-2500 nm	390-2510 nm	380-2500 nm
Spectral sampling	~6.39/11.69 nm	~9.20/9.14 nm	~4.29/8.42 nm	~7.44 nm
Spectral resolution	~7.84/9.53 nm	~11.34/12.24 nm	~4.38/8.25 nm	~8.65 nm
# Spectral samples	224	240	330	285
Spatial resolution	30 m	30 m	30 m	60 m
# Spatial samples	1000	1000	2000	1242
Reference	Storch et al. (2023)	Cogliati et al. (2021)	Yinnian et al. (2020b)	Thompson et al. (2024)

The EnMAP spaceborne imaging spectroscopy mission, led by the German Aerospace Center (DLR), was launched in April 2022 and underwent its commissioning phase (CP) through November 1, 2022 (Baur et al., 2023). During the CP, the scientific team continuously monitored the degradation of various parameters over time until they became essentially stable. The in-flight spectral calibration is performed biweekly using a spectral integrating sphere coated with doped diffuser material (Baur et al., 2019). The spectral smile effect of EnMAP is reported to be small and the nominal CW smile can be derived from a fourth-order polynomial that describes the wavelength variations of each detector across the field of view in the cross-track direction. The EnMAP data used in this study are all acquired between 2023 and 2025 over Niger (21.04-21.81°N, 10.25-10.87°E), a region previously used by Roger et al. (2024) for their relatively homogeneous surface.

The PRISMA spaceborne imaging spectroscopy mission, led by the Italian Space Agency (ASI), was launched in March 2019 and underwent its CP through January 2020. Unlike EnMAP, which uses an integrating sphere for spectral calibration, PRISMA employs lookup tables to correlate optical bench temperature with CW and FWHM shifts, as prism-based spectrometers are significantly affected by temperature (Labate et al., 2009; Cogliati et al., 2021). The PRISMA data used in this study are all acquired between 2021 and 2025 over Sudan (21.45–22.47°N, 27.58–28.75°E), a region previously used by Guanter et al. (2021).

The GF-5 was China's first remote sensing satellite designed for comprehensive atmospheric and surface hyperspectral observations (Yinnian et al., 2020b). It was launched in May 2018 and officially decommissioned in March 2021. Subsequently, GF-5 02 (also known as GF-5B) and GF-5 01A (also known as GF-5A) were launched in September 2021 and December 2022, respectively (Li et al., 2024; Han et al., 2024). All GF-5 series satellites carry the AHSI payload with similar key design parameters, including swath width, spectral measurement range, and number of bands. In this work, we analyze only GF-5A AHSI observations acquired over Saudi Arabia (19.56–20.27°N, 49.08–50.94°E).

The EMIT spaceborne imaging spectroscopy mission, led by NASA's Jet Propulsion Laboratory (JPL), was launched in July 2022 and is installed on the International Space Station (ISS). Unlike EnMAP, PRISMA, and GF-5 AHSI, which employ dual-spectrometer designs to cover the 400-2500 nm range, EMIT achieves this full spectral coverage using an F/1.8 Dyson spectrometer (Green et al., 2020). Diverging from contemporary instruments, EMIT does not carry onboard shutters or calibration mechanisms. Instead, its design philosophy emphasizes alternative calibration approaches through a simplified optomechanical layout. Notably, EMIT was the first to implement on-orbit focal plane array (FPA) calibration, eliminating micron-level FPA rotation (Thompson et al., 2024). The EMIT data used in this study are all acquired between 2023 and 2025 over Saudi Arabia.

3. Sensitivity analysis

3.1. Calibration sensitivity to different sectors

The calibration algorithm relies on some assumed input (e.g., atmospheric state and surface characteristics) to calculating atmospheric parameters in Eq.(2). To evaluate the sensitivity of the calibration algorithm to uncertainties in column concentrations of absorbing gases (H_2O, CH_4, and CO_2), visibility (used to indirectly represent aerosol optical thickness; Guanter et al. 2007), surface pressure, and atmospheric profiles (including temperature and pressure), a total of 105 radiance spectra were generated based on the given libRadtran inputs, as shown in Table 2. True values are used as libRadtran inputs to generate synthetic radiance spectra, while assumed values serve as calibration algorithm inputs for calculating atmospheric parameters. When the assumed values deviate from the true values, the algorithm may incorrectly adjust the spectral parameter to compensate for these discrepancies. This analysis focuses on the sensitivity to individual factors separately. For instance, when examining the impact of carbon dioxide uncertainty, all other libRadtran input parameters are kept identical to their corresponding calibration inputs. Constant 2-nm shifts in both CW and FWHM were added into EnMAP's spectral parameter as the true spectral parameter.

Fig.2 presents the sensitivity of the calibration algorithm to uncertainties in each input factor. Only results for Window A and Window E are selected here for demonstration to represent the VNIR and SWIR spectral regions, as well as scattering-dominated and absorption-dominated windows. Furthermore, these two windows can be used for subsequent NO_2 (Borger et al., 2025) and CH_4 retrievals (Roger et al., 2024). The results for the remaining three windows can be found in the Fig.S4.

For Window A, the calibration errors in both CW and FWHM are generally low, with most values within ±0.01 nm for CW and ±0.005 nm for FWHM. The impact of various factors on the calibration algorithm depends primarily on whether and how they cause changes in the TOA radiance spectra. carbon dioxide and methane have negligible absorption in this spectral range and therefore show almost no impact on the calibration algorithm, while water vaper exhibits weak absorption features in this window. Although visibility variations also alter the radiance spectrum through Mie scattering effects, the polynomial fitting employed

Table 2: Summary of input parameters: libRadtran settings for generating the synthetic radiance spectra and corresponding inputs for the calibration algorithm. $\mathcal{N}(\mu, \sigma^2)$ denotes normally distributed random numbers with mean μ and standard deviation σ. The simulations assume a surface albedo of 0.3 and nadir geometry (solar zenith angle = viewing zenith angle = 0°).

Factor	Assumed value	True value	Unit	Number
CO_2	420	$\mathcal{N}(420, 5^2)$	ppm	20
CH_4	1900	$\mathcal{N}(1900, 50^2)$	ppb	20
H_2O	20	$\mathcal{N}(20, 5^2)$	mm	20
VIS[1]	20	$\mathcal{N}(20, 5^2)$	km	20
PRE[2]	1013	$\mathcal{N}(1013, 3^2)$	hPa	20
ATM[3]	MS	MS,MW,SS, SW,T,US	/	5
				Total: 105

[1] VIS: visibility
[2] PRE: surface pressure
[3] MS: midlatitude summer; MW: midlatitude winter; SS: subarctic summer; SW: subarctic winter; T: tropical; US: U.S. standard atmosphere 1976.

in the calibration algorithm can account for this to some extent, resulting in minimal impact. Changes in surface pressure also modify the radiance spectrum through Rayleigh scattering. However, the assumed uncertainty of 3 hPa is insufficient to introduce significant calibration errors. The atmospheric profile variations affect calibration accuracy primarily by influencing multiple scattering paths.

For Window E, the impact of various factors on FWHM calibration is substantially larger than on CW calibration. Carbon dioxide exhibits no absorption in this spectral range (see Fig.1), and consequently, its concentration uncertainty has negligible effect on both CW and FWHM calibration. In contrast, methane exhibits significant absorption in this range, and this window is commonly used for methane retrieval(Jacob et al., 2022). Methane concentration variations primarily affect the depth of absorption features rather than their spectral positions, thus mainly influencing FWHM calibration, with overestimation of methane concentration leading to overestimation of FWHM. The same principle applies to water vapor. Due to the strong absorption of water vapor, an uncertainty of 5 mm can cause FWHM differences of up to 0.75 nm relative to the true shift. This emphasizes the importance of accurately estimating water vapor column content prior to spectral calibration. Additionally, since scattering effects are weak in this spectral region, the uncertainty in visibility has negligible impact on calibration accuracy. Surface pressure changes can be essentially interpreted as variations in the total number of methane and water vapor molecules, resulting in a slight influence on FWHM calibration. Atmospheric profile variations, which refer to differences in temperature and pressure profiles, affect calibration through multiple mechanisms. Air density exhibits temperature dependence even under constant surface pressure conditions. Furthermore, the absorption cross-sections of methane and water vapor are subject to the temperature and pressure.

The above simulation and calibration results assume a surface albedo of 0.3. However, reflectance varies significantly across different surface types, as shown in Fig.3. Even for

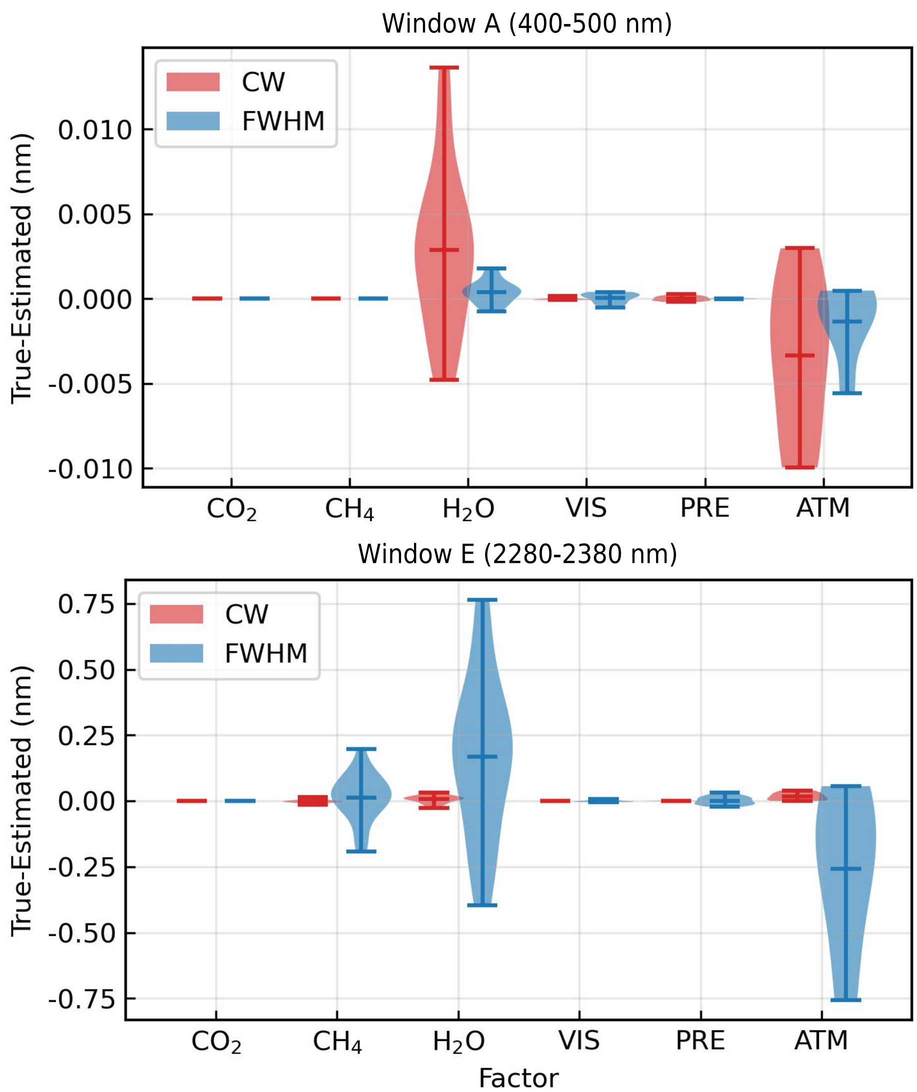

Figure 2: Impact of different factors individually on the spectral calibration algorithm. The true CW and FWHM shifts are both 2 nm relative to EnMAP's nominal spectral parameter. The settings and abbreviations of each factor are shown in Table 2.

bare soil, reflectance is influenced by multiple factors, including soil moisture, particle size composition (sand, silt, and clay proportions), surface roughness, and the presence of iron oxides and organic matter, all of which modify the overall reflectance response. To assess the calibration algorithm's sensitivity to surface reflectance characteristics and varying spectral shifts, 54 radiance spectra were generated based on 6 different surface types (Fig. 3) and 9 sets of spectral shifts. For simplicity, CW and FWHM shifts were kept consistent, ranging from -2 nm to 2 nm at 0.5 nm intervals. Except for surface reflectance, all calibration input parameters remained consistent with the libRadtran inputs. The calibration results for the six surface types are presented in Fig.4.

For Window A, the algorithm demonstrates good overall performance for both CW and FWHM calibration across all spectral shifts and surface types. Minor errors occur over grass

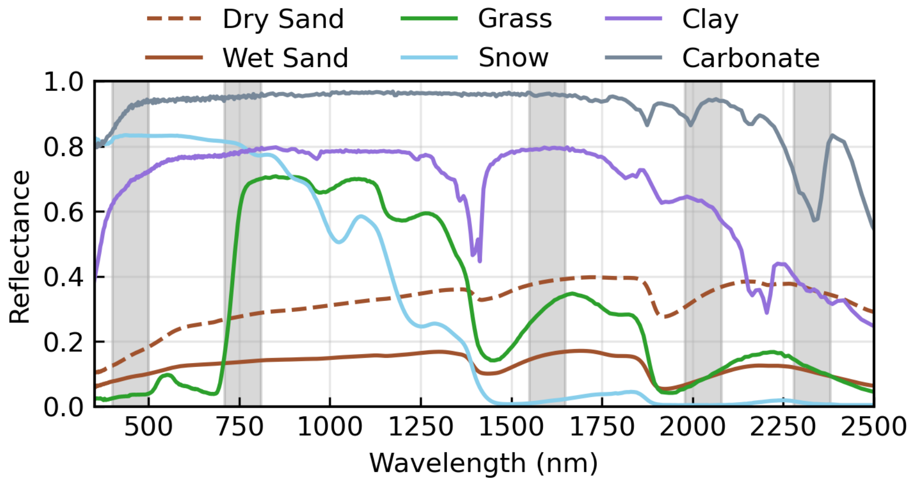

Figure 3: Six representative surface reflectance spectra provided by USGS spectral library. The gray shaded areas indicate several available calibration windows, consistent with Fig.1.

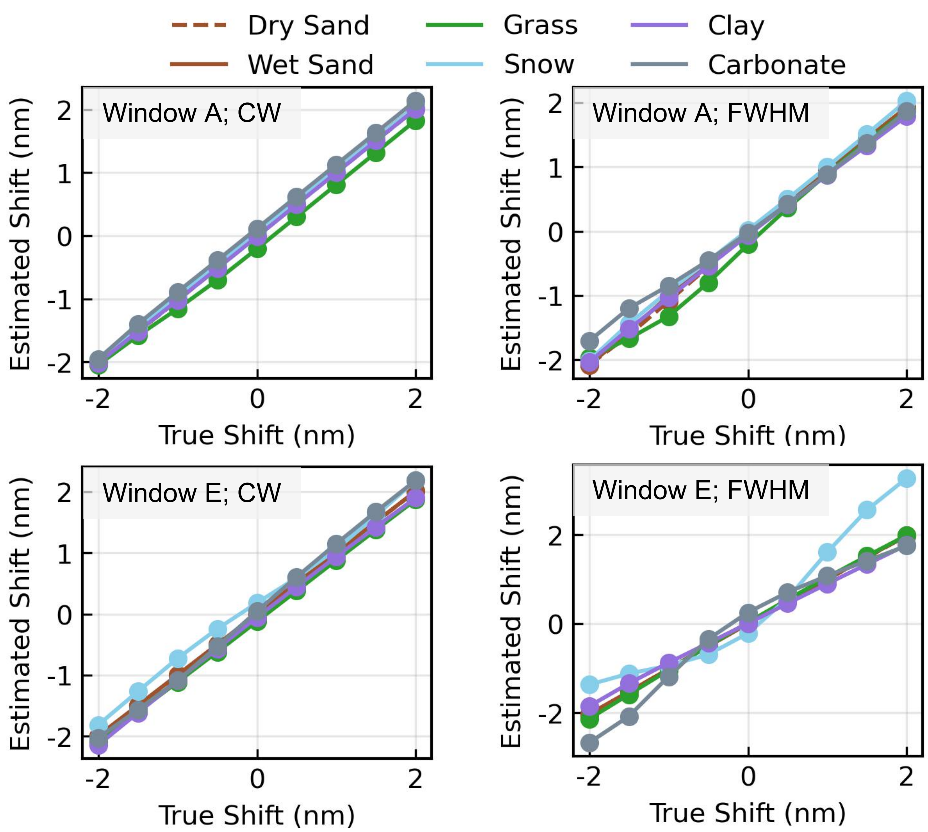

Figure 4: Comparison of true and estimated spectral parameter shifts for six surface types.

and carbonate surfaces, primarily because the reflectance characteristics of these two surface types cannot be perfectly modeled by the Legendre polynomials in Equation (3), resulting in erroneous adjustments of CW and FWHM as compensation. The same phenomenon and underlying cause are observed in Window E.

For Window E, CW calibration exhibits only minor errors over snow and carbonate surfaces, with differences from the true shift values consistently below 0.5 nm. In contrast, FWHM is more susceptible to erroneous adjustment as compensation, particularly over snow surfaces, where the calibrated shift exceeds the true value by approximately 1 nm when the true shift is 2 nm. The greater robustness of CW calibration stems from the presence of multiple spectral features caused by gas absorption within this window. The reduced accuracy over carbonate and snow surfaces is primarily due to the pronounced and highly non-linear absorption features associated with carbonate ions (CO_3^{2-}) and solid-phase H_2O within the 2280-2380 nm spectral region. The increased sensitivity of FWHM calibration reflects the algorithm's greater difficulty in accurately characterizing spectral band broadening compared to center wavelength shifts when surface reflectance cannot be adequately represented by the polynomial fitting approach. Overall, our algorithm is suitable for surfaces whose reflectance exhibits linear variations within the calibration window. When surfaces present significant nonlinear absorption features that cannot be adequately modeled by polynomials, spectral calibration may produce inaccurate estimates, particularly for FWHM calibration. Therefore, in practical implementation, scenes with spectrally flat reflectance should be preferentially selected as input. Beyond EnMAP's spectral parameter, we analyzed other instruments such as PRISMA and reached similar conclusions.

For calibration window width selection, we have tested other widths in addition to 100 nm. Notably, spectral shifts across different channels are not consistent, with on-orbit calibration results from doped spheres indicating variations within $\sim$0.2 nm depending on across-track position. Our algorithm's calibration result represents the average shift of all channels within the window. While narrower windows allow the Nelder-Mead algorithm to converge even when unknowns exceed spectral bands, they provide insufficient observational information, causing high sensitivity to the prior state vector and instability in Eq.(6) minimization. Conversely, wider windows reduce the representativeness of averaged shifts across the spectral range while increasing sensitivity to surface reflectance. Therefore, the selection of window width requires a trade-off and should consider the width of subsequent retrieval (e.g., methane) windows. The averaged shift approach has been widely adopted in studies by Guanter et al. (2021), Roger et al. (2024), and etc. Alternatively, Thompson et al. (2018b) represent wavelength shift as a channel-dependent function using cubic splines with inflection points defined by the second derivative of wavelength dispersion.

3.2. Gas Retrieval Sensitivity to Calibration

Gas retrieval algorithms for imaging spectrometers can be broadly categorized into two types: pixel-wise and column-wise (Ayasse et al., 2023). Representative algorithms of the former include the iterative maximum a posteriori – differential optical absorption spectroscopy (IMAP-DOAS) (Frankenberg et al., 2005; Cusworth et al., 2023), while representative algorithms of the latter include the matched filter (MF), lognormal matched filter (LMF), and their slight variations (Thompson et al., 2015; Foote et al., 2020; Pei et al., 2023). The IMAP-DOAS algorithm starts modeling from solar incident radiation and retrieves methane column concentration (XCH_4) through iterative nonlinear optimization. Since rigorous forward models require accurate channel positions, CW shifts are typically included in the state vector as adjustable parameters. Column-wise algorithms begin modeling from column-averaged spectra, employing a simplified linear forward model to derive enhancements relative to background column concentrations. Guanter et al. (2021) analyzed ΔXCH_4 retrieval errors under two spectral shift combinations for PRISMA, which have shown a peak systematic error of about 10%. However, in most other applications employing column-wise algorithms, spectral characterization has not been considered a necessary prerequisite for gas retrieval. Here we use synthetic data to comprehensively evaluate the impact of spectral shifts and channel broadening on the column-wise algorithm. LMF was selected for the evaluation due to its robustness across different concentration enhancement scenarios.

In column-wise algorithms, one of the key parameters is the unit absorption spectrum, which is jointly determined by the gas absorption cross-section, the CW list, and the FWHM list. Fig.5 presents the unit absorption spectra corresponding to various spectral shifts and channel broadening, calculated using the lookup table provided by Foote et al. (2021). Spectral shifts cause a horizontal displacement of the unit absorption spectrum and are accompanied by slight changes in its shape. In contrast, channel broadening has minimal impact on the position of absorption features but changes their depth. A smaller FWHM corresponds to a finer spectral resolution, thereby revealing richer features in the unit absorption spectrum.

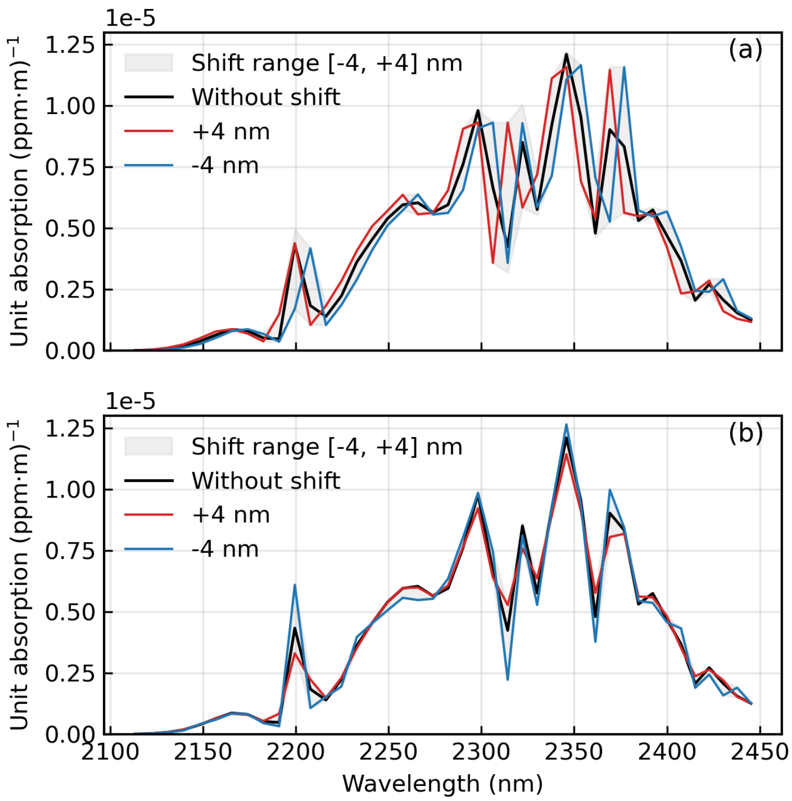

Figure 5: Unit absorption spectra under (a) different spectral shifts and (b) different channel broadenings, computed from the lookup table provided by Foote et al. (2021). The shifts for both CW and FWHM range from -4 nm to 4 nm. The CW and FWHM lists are from EnMAP. For satellite-observed total column concentrations, 1 ppm · m corresponds to approximately 0.125 ppb (Thompson et al., 2016).

On the one hand, we selected EnMAP plume-free imagery and simulated radiance in the presence of ΔXCH_4 to analyze single-pixel concentration retrieval sensitivity to CW and FWHM shifts, following Guanter et al. (2021). With spectral shifts and channel broadening ranging between [-2, 2] nm, retrieval errors are evaluated against reference results obtained without shifts (using true wavelength parameters), as shown in Fig.6. Under zero CW shift conditions, negative channel broadening (true FWHM < nominal FWHM) causes slight ΔXCH_4 overestimation when using nominal parameters, while positive broadening leads to underestimation. Under zero FWHM shift conditions, any spectral shift consistently produces ΔXCH_4 underestimation, which intensifies with increasing channel broadening. For instance, 1 nm channel broadening with 1 nm spectral shift yields ∼60 ppb (6%) underestimation, while 2 nm broadening with ∼2 nm shift results in up to 200 ppb (20%) underestimation. The following section will demonstrate the CW and FWHM shifts in the across-track direction for various spaceborne imaging spectrometers, where larger shifts typically occur at the edges of the swath. This implies that if methane plumes happen to appear at the edges in the across-track direction, ΔXCH_4 retrievals will likely suffer from underestimation. Additional simulations conducted on other spaceborne instruments and pixels at different coordinates show varying retrieval errors, but the overall trends are comparable.

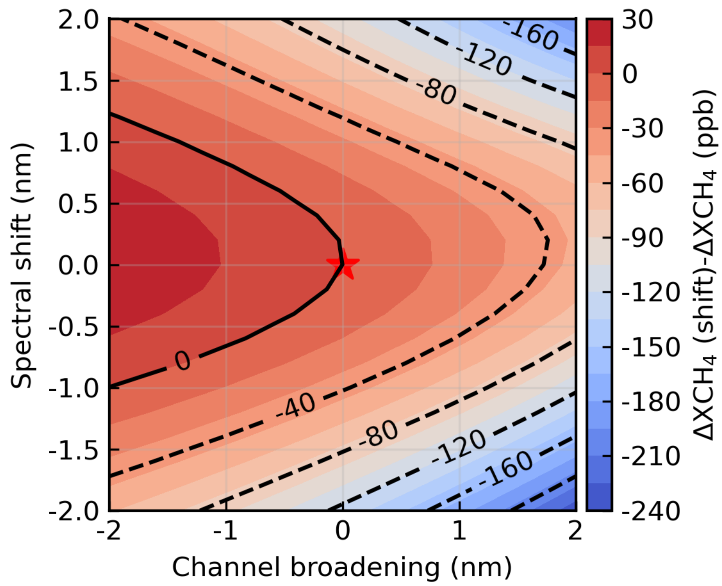

Figure 6: ΔXCH_4 retrieval error as a function of spectral shift and channel broadening. The reference case (no shift) is marked with a red star. This analysis is based on EnMAP plume-free imagery. The true ΔXCH_4 used in the simulation is 1000 ppb.

On the other hand, we also selected real EnMAP plume-containing imagery to analyze the sensitivities of ΔXCH_4 retrieval and integrated mass enhancement (IME) to CW and FWHM shifts. The point source corresponds to Kazakhstan's Karaturun East oil field, reported by Guanter et al. (2024) as a record-breaking methane leak. Comparative methane plume retrievals using unshifted versus shifted wavelength parameters are shown in the Fig.7. Note that CW and FWHM values provided by EnMAP are treated as the reference (unshifted) wavelength parameters in this analysis.

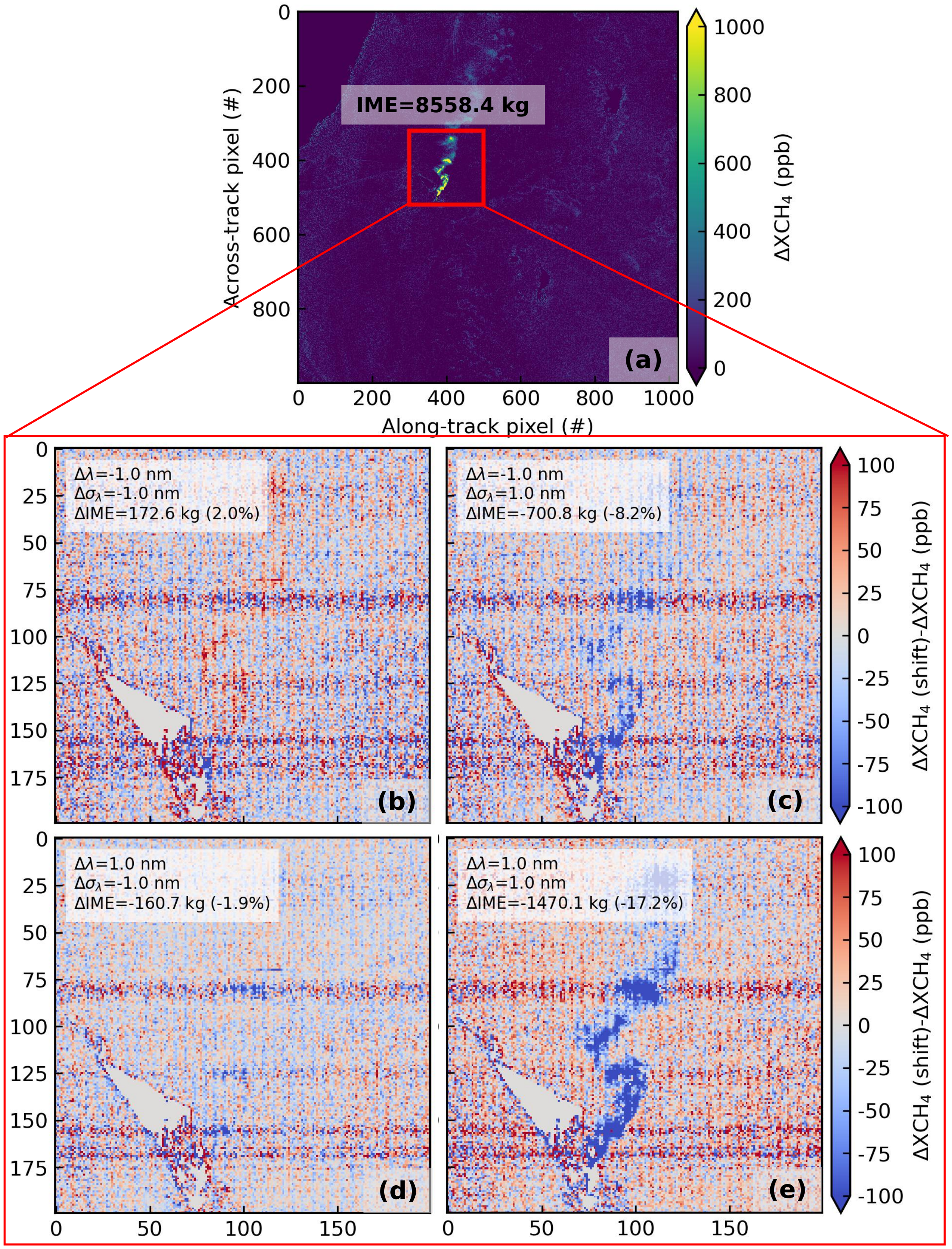

Figure 7: Comparative methane plume retrievals using unshifted versus shifted wavelength parameters. $\Delta\lambda$ and $\Delta\sigma_\lambda$ represent CW shift and FWHM shift, respectively. This analysis is based on EnMAP plume-containing imagery. Data source: EnMAP (Scene ID: 20230923T081549Z_002_V010502)

In addition, the single-pixel ΔXCH_4 retrieval sensitivity result presents comparable error patterns with Fig.6, as shown in the Fig.S5. Furthermore, Fig.8 presents the IME retrieval error as a function of spectral shift and channel broadening. The observed asymmetry relative to Fig.6 is attributed to EnMAP's intrinsic CW and FWHM shifts, which vary across spectral channels. The same procedure was also applied to plume-containing PRISMA imagery with more severe shifts, where this asymmetry along the spectral shift axis is more pronounced. The retrieved IME of the masked plume using unshifted wavelength parameters is ∼8558 kg. Under conditions of spectral shift and channel broadening, systematic underestimation predominates. In the most extreme case (2 nm channel broadening and 2 nm spectral shift), IME underestimation reaches 3200 kg (37%). This finding highlights the essential role of spectral calibration in accurate methane emission quantification.

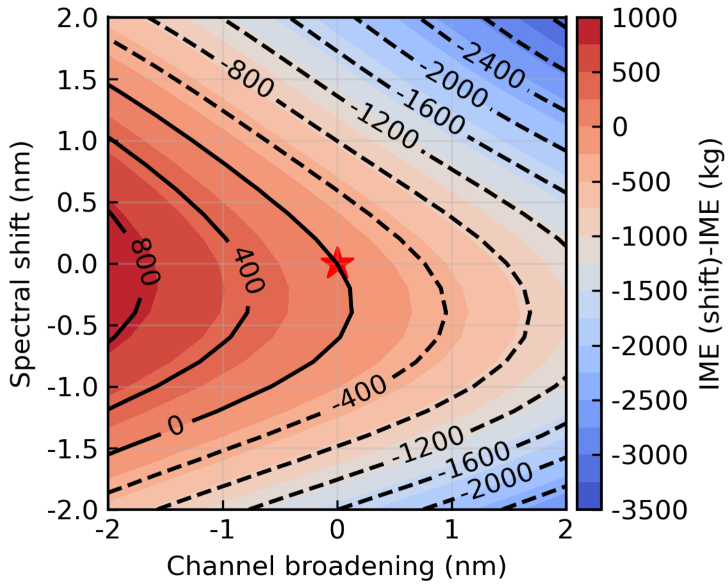

Figure 8: The integrated mass enhancement (IME) retrieval error as a function of spectral shift and channel broadening. The reference case (no shift) is marked with a red star. This analysis is based on EnMAP plume-containing imagery. The retrieved IME using unshifted wavelength parameters is 8558 kg.

4. Calibration results

4.1. EnMAP

Nominal CW (mean and smile) and FWHM (only mean) provided in the EnMAP metadata are compared with algorithm-estimated values (with 1-σ uncertainty) based on the scene collected on July 2, 2024, as shown in Fig.9. Only Window A and Window E are shown here as representative cases. Fig.9(a) and (b) show the spectral shift and channel broadening for channel #1, which represents the VNIR spectrometer. The estimated CW shows a similar upward trend to the nominal smile. A systematic spectral shift of ∼0.36 nm (averaged over the across-track direction) and a peak-to-peak (P2P) difference in CW of ∼0.37 nm are found in this scene. The "frown" pattern can be seen in Fig.9(b). The systematic channel broadening (averaged over the across-track direction) and the P2P difference in FWHM are 0.94 nm and 0.72 nm, respectively.

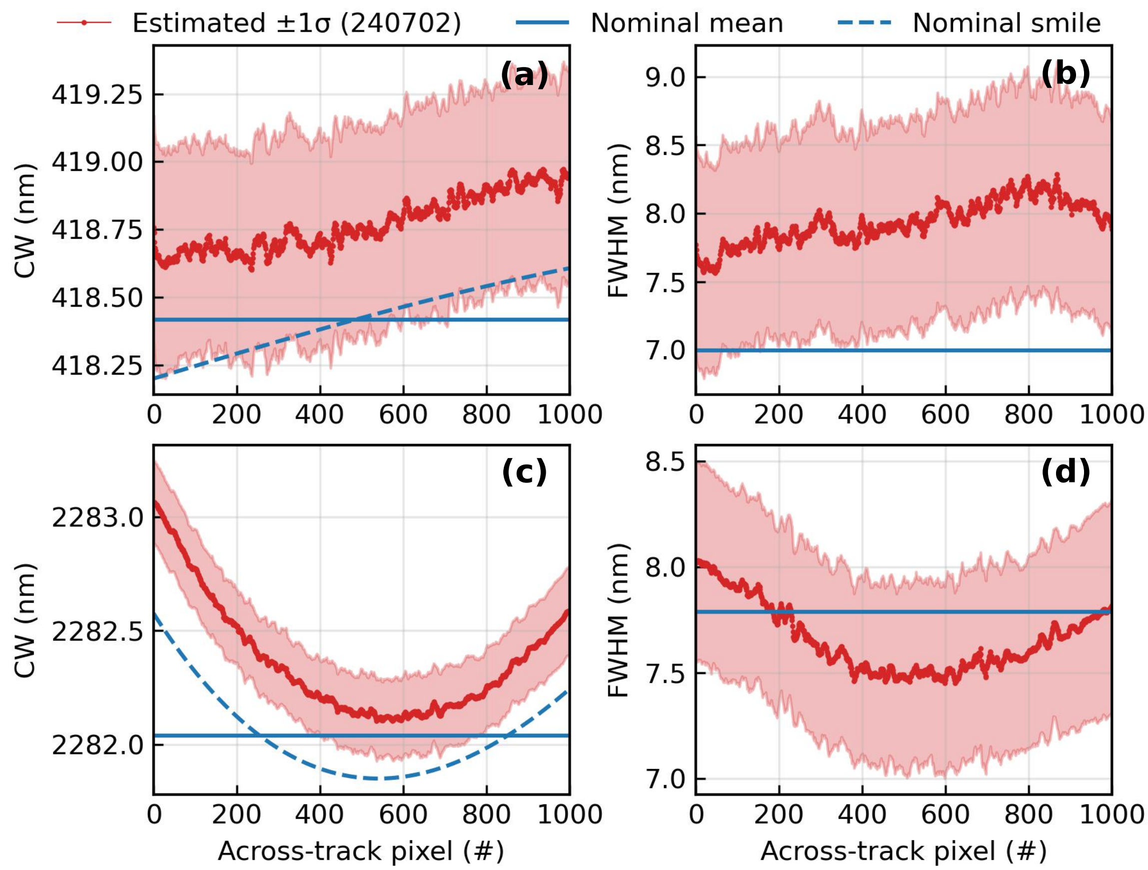

Figure 9: Estimated and nominal EnMAP spectral parameters (CW and FWHM) in the across-track direction for Window A (top) and Window E (bottom) at selected channels. The solid lines represent the spectral parameter estimated by the scene-based spectral calibration algorithm, the dashed lines represent the nominal smile, and the dotted lines represent the nominal lines.

Fig.9(c) and (d) show the spectral shift and channel broadening for channel #203, representing the SWIR spectrometer. The estimated CW shows a similar trend to the nominal smile. The estimated CW and nominal smile show a better correspondence compared to the VNIR, although overall upward shifts are observed. The misalignment between them consistently remains within 0.5 nm across all across-track pixels. The systematic spectral shift and the P2P difference in CW are 0.33 nm and 0.96 nm, respectively. The smile effect is also evident in the estimated FWHM, exhibiting -0.13 nm systematic channel broadening and 0.58 nm P2P difference.

Concerning the 1-σ calibration uncertainties, Window E exhibits lower uncertainty than Window A, and CW calibration shows lower uncertainty than FWHM. These uncertainties are mainly governed by three factors: the sensitivity of observed radiance spectra to CW and FWHM variations (characterized by the Jacobian matrix), measurement noise, and forward model errors. Window E benefits from multiple atmospheric absorption features, while Window A contains only two solar Fraunhofer line features. The greater number of absorption features enhances spectral sensitivity to CW shifts. Furthermore, Window A's susceptibility to scattering effects means that inaccurate atmospheric assumptions introduce forward model errors that propagate into calibration uncertainties. Conversely, modeling for Window E is more accurate, which is reflected in the good agreement between simulated and observed radiance spectra (see Fig.S6).

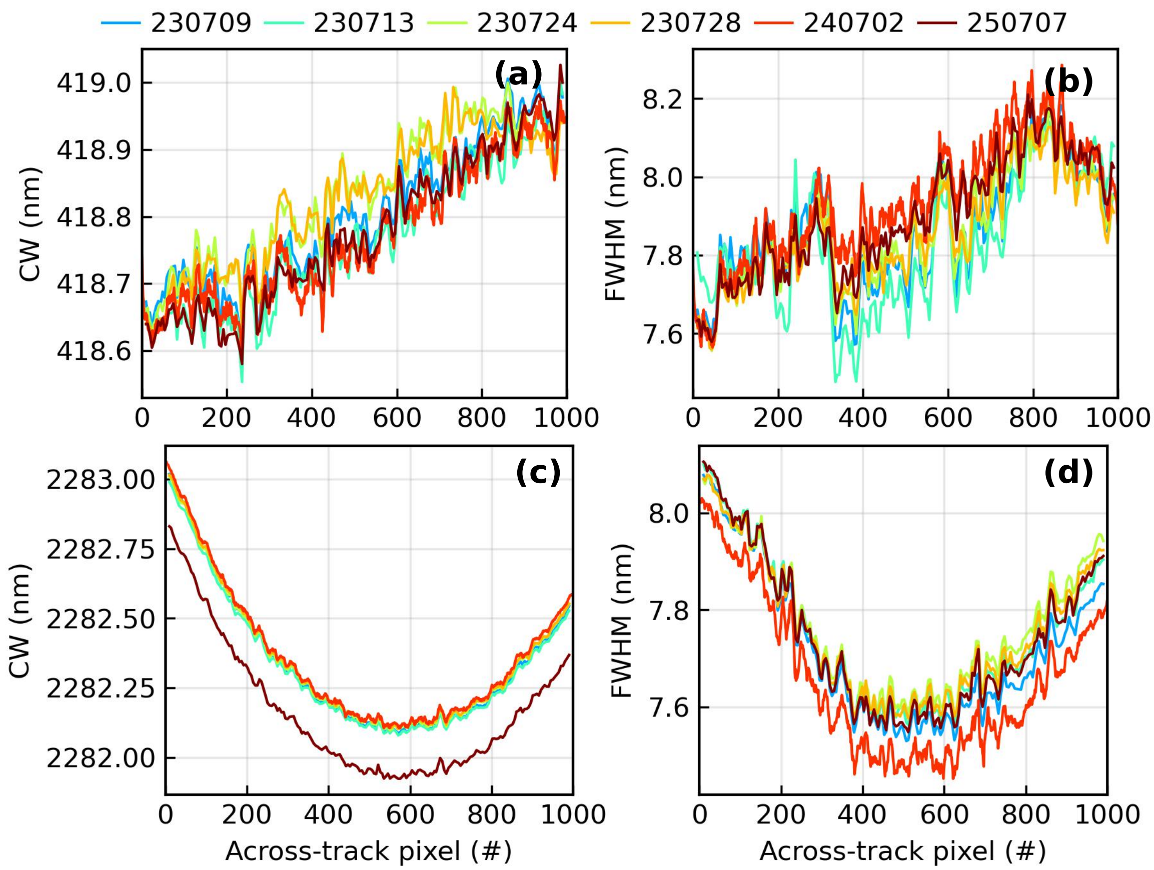

Figure 10: Estimated EnMAP spectral parameters in the across-track direction for Window A (top) and Window E (bottom) at selected channels. Colors denote different observation dates. 200 across-track sample pixels were used for calibration to reduce computation time.

Fig.10 presents calibration results from multiple dates spanning nearly two years, revealing instrumental spectral response degradation patterns. Window A calibration results shown in Fig.10(a) and (b) demonstrate significantly greater temporal variability compared to Window E. Beyond potential instrumental degradation effects, we attribute this variability to Window A's inherently higher calibration uncertainty. As demonstrated in Fig.9, Window A calibration naturally exhibits larger uncertainties due to its spectral characteristics and modeling challenges. Furthermore, all observation dates display a consistent jagged pattern, suggesting that this behavior stems from detector-related issues or imperfect relative radiometric calibration rather than variations in surface properties or atmospheric conditions. The anomalous bulge observed between pixels 200-350 in Fig.10(b) has been similarly reported regarding EnMAP VNIR response non-uniformity (Storch et al., 2023). In contrast, the algorithm obtained nearly consistent CW results in the SWIR, except for July 7, 2025. This indicates the stability of the SWIR spectrometer within one and a half years after the CP phase and the robustness of the calibration algorithm in Window E. Furthermore, results indicate that the SWIR spectrometer most likely underwent degradation after July 7, 2024, resulting in systematic spectral shifts. Compared to CW calibration, FWHM calibration results are less stable, even for the first 5 dates, which is consistent with the uncertainty conclusions shown in Fig.9.

Storch et al. (2023) employed doped sphere calibration to characterize spectral shifts across various bands in the cross-track direction. Their results at 2257 nm shows a P2P difference in CW of $\sim$0.7 nm, with the left edge being about 0.35 nm higher than the right edge. Roger et al. (2024) presented scene-based spectral calibration results using data collected in Niger during the CP. The methodological similarities include polynomial-based surface reflectance modeling and at-sensor radiance fitting. The key distinction is our algorithm's more rigorous forward model that incorporates scattering and absorption coupling effects, though such coupling is minimal within the SWIR range. The aforementioned calibration studies all demonstrate consistent findings, despite representing spectral shift conditions from different observation dates.

Furthermore, since November 18, 2024, SWIR corrections have been implemented at the L1B level to reduce SWIR across-track striping noise and random noise (EnMAP, 2024). Our algorithm was applied to different versions (before and after implementation) of the same observation scene, and results show that calibration results based on the latest-version data are smoother, as shown in the Fig.S7.

4.2. PRISMA

Nominal CW (mean and smile) and FWHM (mean and smile) provided in the PRISMA metadata are compared with algorithm-estimated values, as shown in Fig.11. A clear temporal trend can be found in Fig.11(a) and (b) for the VNIR. The gradual drift during operation could be attributed to the combined effects of thermal cycling, optical surface contamination, and exposure to ultraviolet radiation (Jaworske, 1999; Tansock et al., 2015). Note that Window A was adjusted to 420-500 nm rather than 400-500 nm due to poor spectral fitting performance in the first few bands. PRISMA L1 data have been reported to suffer from instrument artifacts or calibration issues in the blue region (Braga et al., 2022; Pellegrino et al., 2023). Even with this narrowed fitting window, Window A calibration results reveal significant systematic spectral shifts (0.77-1.28 nm) and channel broadening (0.98-1.94 nm) across all the date. Therefore, PRISMA data may not be suitable for the detection and quantification of NO_2 which requires high-quality VNIR radiance spectra.

In contrast, there is no clear temporal trend in the SWIR, as shown in Fig.11(c) and (d). During the period from August 2021 to July 2023, systematic spectral shifts exhibited variations between 0.20 and 0.07 nm, while systematic channel broadening showed variations between 0.77 and 1.12 nm, relative to nominal mean values. Moreover, the left portion performed better than the right portion in the across-track direction. In the last two dates, the estimated CW and FWHM show clear differences in both shape and magnitude compared to those from the first four dates. The degradation in the SWIR is evident not only in

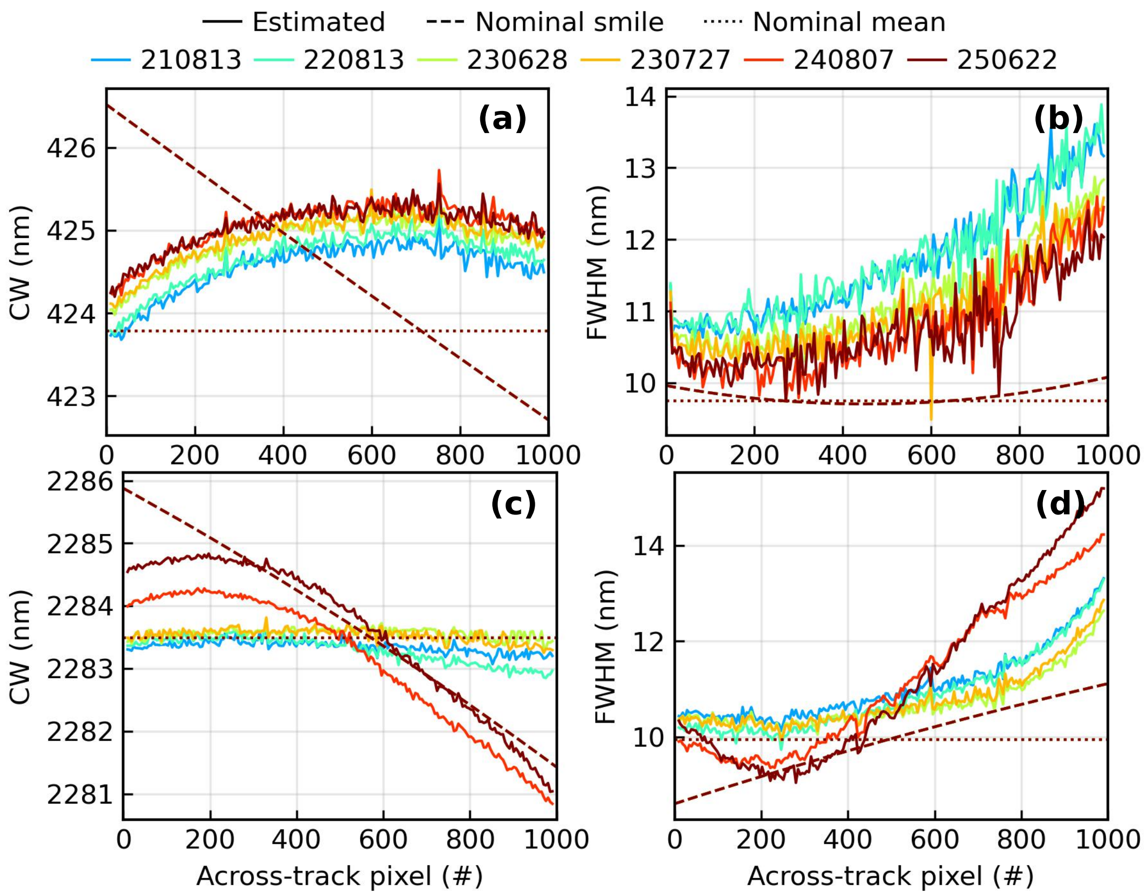

Figure 11: Estimated and nominal PRISMA spectral parameters in the across-track direction for Window A (top) and Window E (bottom) at selected channels. The solid lines represent the values estimated by the scene-based spectral calibration algorithm, the dashed lines represent the nominal smile, and the dotted lines represent the nominal mean. Colors denote different observation dates. 200 across-track sample pixels were used for calibration to reduce computation time.

window E but also in window D, as shown in Fig. S8. Therefore, regular in-flight calibration is required to monitor spectral performance during mission operations. This also highlights the critical importance of column-wise processing to minimize cross-track non-uniformity impacts on retrievals.

PRISMA's nominal smile, derived from optical bench temperature inference, appears less reliable in its across-track trends compared to EnMAP. Guanter et al. (2021) previously used scene-based spectral calibration algorithms to estimate CW and FWHM in the across-track direction. Our algorithm yielded similar trends when using the same observation scene in the same version (V3.6). We also noticed that Guanter et al. (2021) employed a redundant flip function when reading PRISMA data, which means the estimated CW and FWHM should be flipped in the across-track direction. Additionally, our study emphasizes the importance of using the latest-version (V4.5-0) data, as the same observation scene in different versions exhibit differences that can cause calibration algorithms to produce markedly different results (see Fig.S9).

4.3. GF-5A AHSI

Fig.12 presents the spectral calibration results from four different dates over approximately one year. The results are generally consistent across all dates, indicating no significant degradation in the instrument's performance during this period. Particularly, the calibration results from the two dates in July 2024 are highly consistent, indirectly reflecting the reliability of the calibration algorithm. In Window A, GF-5A AHSI demonstrates excellent across-track uniformity with minimal variability. As shown in Fig.12 (a) and (b), the P2P differences in both CW and FWHM remain below 0.1 nm across all observation dates. The systematic spectral shifts range from 0.05 to 0.13 nm, and systematic channel broadening varies between 0.44 and 0.49 nm across all dates. This low across-track variability in the VNIR indicates good spectral stability and suggests that GF-5A AHSI's VNIR detector exhibits minimal spatial non-uniformity in its spectral response.

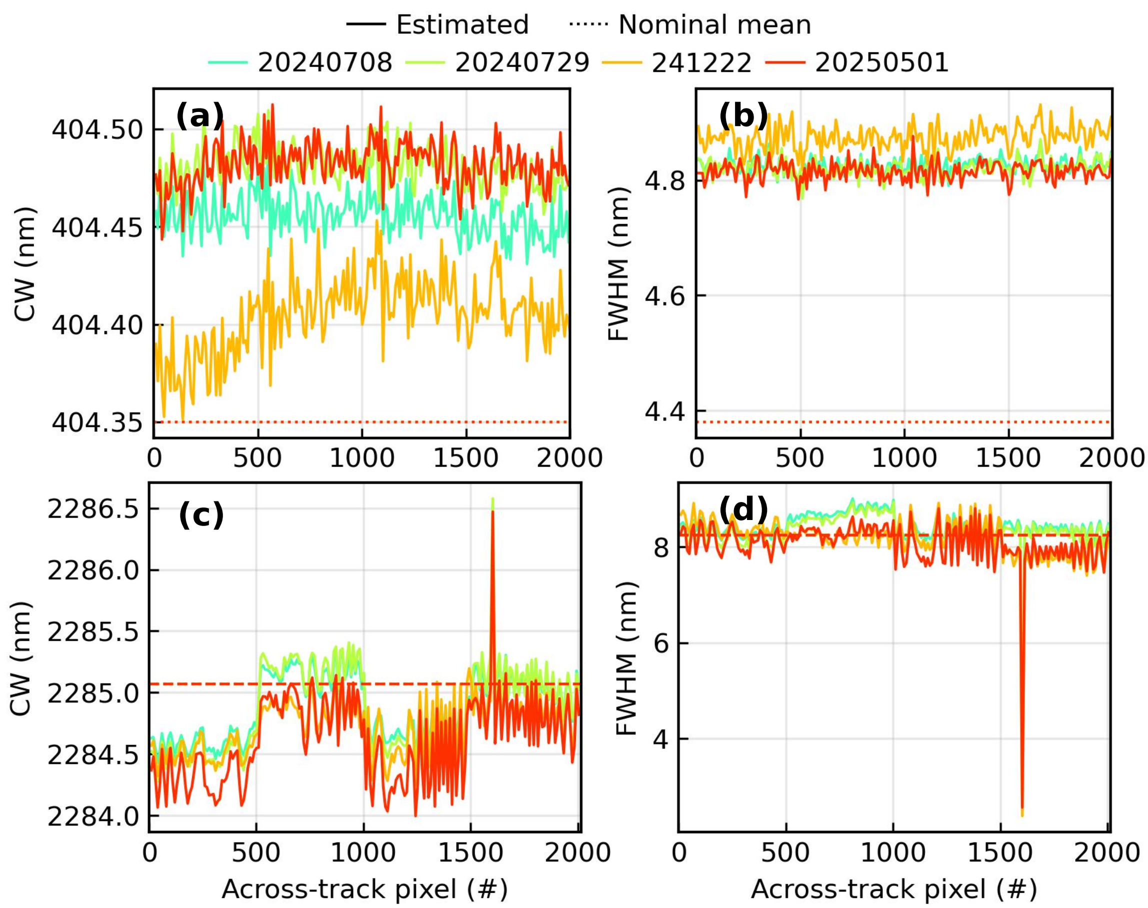

Figure 12: Estimated and nominal GF-5A AHSI spectral parameters in the across-track direction for Window A (top) and Window E (bottom) at selected channels. The solid lines represent the values estimated by the scene-based spectral calibration algorithm, the dashed lines represent the nominal smile, and the dotted lines represent the nominal mean. Colors denote different observation dates. 200 across-track sample pixels were used for calibration to reduce computation time.

Fig.12(c) and (d) also demonstrate segmented variations within Window E. While individual detector segments show relatively low across-track variability, inter-segment CW variations can reach up to 1 nm. There is an obvious anomalous pixel (near #1600), with all observation dates showing anomalies for this pixel, suggesting that the detector element corresponding to this pixel may have issues. Taking the calibration results from May 1, 2025 as an example, the P2P differences in CW and FWHM are 1.16 nm and 1.34 nm, respectively, which are generally consistent with the conclusions (better than 1 nm) introduced by Yinnian et al. (2020b). Regarding systematic shifts, the wavelength shift is approximately -0.46 nm, and the channel broadening is approximately -0.15 nm.

Fig.S10 presents the spectral calibration results of GF-5A AHSI in early on-orbit operation (February 2023, two months post-launch during the CP), when the nominal spectral parameters still remained the laboratory calibration results. A discrepancy exceeding 6 nm existed between the nominal CW and the estimated values. This result reveals the significant spectral shift phenomenon occurring after the imaging spectrometer's launch, while emphasizing the importance of using scene-based calibration algorithms for preliminary data inspection. Additionally, this figure reveals a "four-segment" variation pattern in the across-track direction, with each segment containing approximately 500 pixels. This segmented pattern exists widely across multiple windows in the SWIR spectral range (e.g., window D in Fig.S11). Essentially, this is due to GF-5(A/B) AHSI's unique adoption of four alternately arranged SWIR detectors to achieve 60 km swath imaging (Yinnian et al., 2020b). Additionally, to our knowledge, the onboard calibrator carried by GF-5 (A/B) AHSI consists of a solar diffuser and a solar diffuser stability monitor, enabling long-term and high-precision calibration. However, it cannot cover the entire field of view (FOV) under solar diffuser observation mode. In contrast, the scene-based spectral calibration algorithm can achieve full FOV calibration.

4.4. EMIT

Nominal CW and FWHM provided in the EMIT metadata are compared with algorithm-estimated values, as shown in Fig.13. As shown in Fig.13(a) and (b), the frown effect is clearly evident in the VNIR region. P2P differences in both CW and FWHM remain below 0.5 nm, excluding obvious outliers. The systematic spectral shifts for the two observation dates are -0.57 nm and 0.42 nm, respectively, while the corresponding channel broadening values are 2.5 nm and 2.36 nm. It should be noted that during the calibration process, we found that the first few bands in EMIT's blue region could not achieve satisfactory fitting with observed spectra even after spectral parameter adjustment (see Fig. S12), presenting issues similar to those observed in PRISMA. Consequently, we excluded these bands and adopted the 420-500 nm range for Window A.

Fig.13(c) and (d) reveal an m-shaped curve pattern, particularly pronounced in the FWHM measurements. Cross-track FWHM deviation has been reported by Thompson et al. (2024), showing similar shape and magnitude to our results. Taking the June 13, 2025 calibration results as an example, the P2P differences in CW and FWHM are approximately 0.4 nm and 1 nm, respectively, demonstrating low across-track dependence when obvious outliers are excluded. The systematic spectral shift and channel broadening are 0.01 nm and -0.34 nm, respectively. Additionally, compared to the EnMAP and PRISMA calibration results presented earlier, EMIT exhibits more pronounced random fluctuations in the across-track direction, indicating that future product processing algorithms should consider approaches

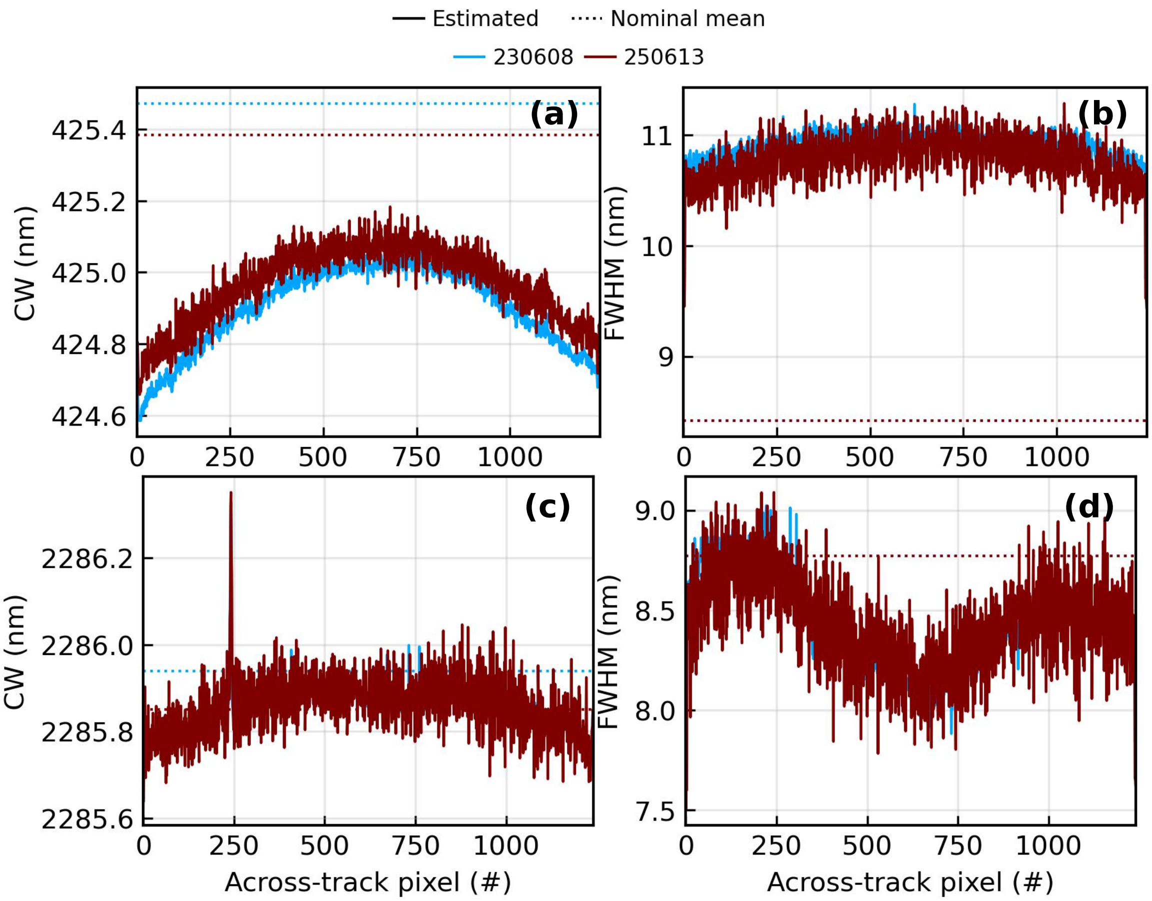

Figure 13: Estimated and nominal EMIT spectral parameters in the across-track direction for Window A (top) and Window E (bottom) at selected channels. The solid lines represent the values estimated by the scene-based spectral calibration algorithm, the dashed lines represent the nominal smile, and the dotted lines represent the nominal mean. Colors denote different observation dates.

to minimize such inconsistencies.

Based on the calibration results of each instrument presented above, Fig.14 compares the relative performance of each instrument across evaluation metrics including systematic spectral shifts, channel broadening, P2P difference in CW and P2P difference in FWHM, with Window A and Window E representing VNIR and SWIR, respectively. Regarding the VNIR region, GF-5A AHSI performs best across all four metrics, exhibiting the smallest cross-track dependence and the least deviation from the nominal values. EnMAP demonstrates balanced overall performance across the 8 evaluation metrics with no obvious weaknesses. EMIT performs best in SWIR spectral shift and P2P difference in CW but exhibits relatively poor performance in VNIR channel broadening. In contrast, PRISMA shows pronounced degradation due to its relatively long time since launch (more than 6 years). According to PRISMA data acquired on 22 June 2025, the SWIR P2P differences in CW and FWHM reached 3.80 nm and 6.15 nm, respectively, and such a high cross-track dependence implies that simply adopting the nominal spectral parameter may introduce considerable errors in subsequent quantitative retrieval studies.

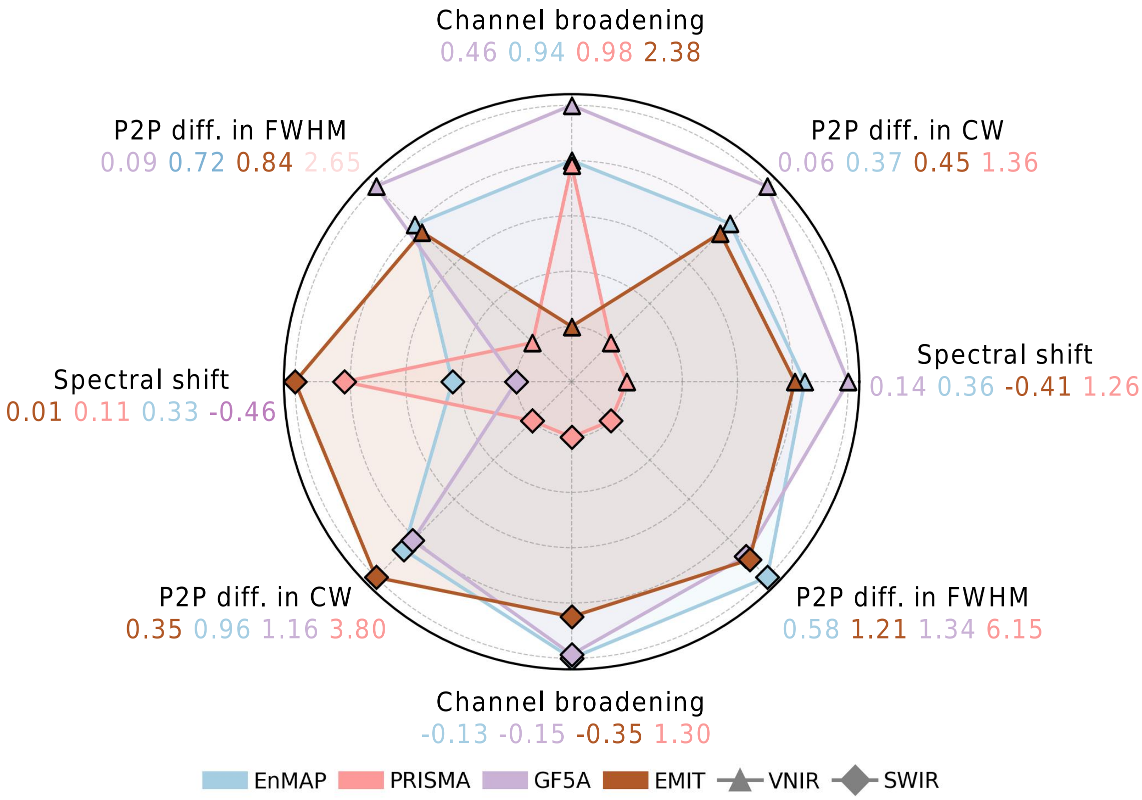

Figure 14: Performance comparison of EnMAP (240702), PRISMA (250622), GF-5A AHSI (250501) and EMIT (250613) imaging spectrometers across eight evaluation metrics. All displayed values are absolute values with units in nm. For all evaluation metrics, smaller absolute values indicate better performance.

5. Discussion

The spectral calibration algorithm presented in this work assumes that the SRF of each spectral channel can be accurately described by a Gaussian distribution. Under this assumption, the retrieved parameters δ_1 (CW shift) and δ_2 (FWHM shift) should be interpreted as effective quantities associated with the Gaussian SRF. In reality, the SRFs of imaging spectrometers deviate slightly from an ideal Gaussian, particularly in the wings, due to stray light scattered by the grating and other elements of the optical system (Thompson et al., 2018a). Such deviations can lead to systematic biases in both CW and FWHM estimates when the true SRF exhibits significant asymmetry or side-lobe structure. In future work, the algorithm could be extended to incorporate measured SRFs from pre-flight laboratory calibration or adopt more flexible parameterizations (e.g., super-Gaussian, Voigt, or instrument-specific empirical functions) to reduce biases arising from this assumption.

Our algorithm relies on accurate atmospheric and surface parameters as inputs to libRadtran simulations. While surface altitude can be reliably obtained from digital elevation models, column concentrations of CO_2 and CH_4 can be derived from OCO-2 or TROPOMI products, and water vapor column content can be obtained directly from satellite L1/L2 products or estimated using the three-channel ratioing technique. Results from both the synthetic data demonstrate that atmospheric profile assumptions can also influence calibration results in certain windows. For example, differences between midlatitude summer and winter profiles produce CW biases in the Window E. This highlights the potential benefit of using location- and time-specific atmospheric profiles from reanalysis datasets such as ERA5 (Hersbach et al., 2020) to reduce calibration uncertainty.

In this study, gaseous absorption was modeled using libRadtran's REPTRAN band parameterization, with spectroscopic data from HITRAN 2004. However, Kukkurainen et al. (2025) showed that libRadtran simulations performed with a line-by-line (LBL) approach yield noticeable differences in transmittance compared to REPTRAN, particularly in the 2000–2500 nm region. These discrepancies can arise from differences in HITRAN versions or in the adopted line broadening functions. Since our spectral calibration in the SWIR, especially in windows D and E, relies on accurately reproducing fine-scale absorption structures, such differences could introduce slight biases in FWHM retrieval. Future work could assess this effect by conducting sensitivity tests with updated spectroscopic databases (e.g., HITRAN 2020) and by comparing REPTRAN against LBL simulations.

6. Conclusion

This study presents a scene-based spectral calibration algorithm for spaceborne imaging spectrometers that operates directly on at-sensor radiance, addressing limitations of previous approaches that rely on surface reflectance retrieval. The algorithm incorporates rigorous atmospheric radiative transfer modeling through libRadtran to account for the coupling between gaseous absorption and atmospheric scattering effects, providing more accurate spectral characterization than simplified approaches.

The sensitivity analysis demonstrates that calibration accuracy depends critically on the spectral window characteristics and input parameter uncertainties. SWIR windows containing multiple atmospheric absorption features (Window E) provide more robust CW calibration than VNIR windows relying primarily on solar Fraunhofer lines (Window A). Water vapor column uncertainty emerges as a particularly significant factor, with 5 mm uncertainty potentially causing FWHM errors up to 0.75 nm in Window E. Surface reflectance characteristics also influence calibration performance, with spectrally non-linear surfaces (grass, carbonate, snow) introducing systematic biases that limit algorithm applicability.

The quantitative assessment of spectral calibration impacts on methane retrieval reveals substantial consequences for trace gas quantification. Spectral shifts and channel broadening may lead to a systematic underestimation (more likely) or overestimation of ΔXH_4, with errors reaching 37% (3200 kg) for integrated mass enhancement calculations under severe miscalibration scenarios. These findings underscore the critical importance of accurate spectral characterization for quantitative atmospheric composition studies and highlight the need for regular in-flight calibration monitoring.

Application of the algorithm to four representative spaceborne imaging spectrometers reveals distinct performance characteristics and temporal evolution patterns. EnMAP demonstrates stable spectral performance with systematic spectral shifts below 0.4 nm and P2P differences under 1 nm in both VNIR and SWIR regions. GF-5A AHSI exhibits excellent across-track uniformity in the VNIR (P2P difference in CW <0.1 nm) and shows segmented variations in the SWIR due to its four-detector mosaic design. PRISMA exhibits significant temporal degradation, particularly evident in SWIR cross-track uniformity, with peak-to-peak differences in CW and FWHM reaching 3.8 nm and 6.15 nm, respectively. EMIT shows characteristic m-shaped patterns in the SWIR with moderate across-track variability.

The comparative performance evaluation across instruments provides valuable insights for the hyperspectral remote sensing community. Newer instruments (EnMAP, GF-5A AHSI, EMIT) generally demonstrate superior spectral stability compared to older missions (PRISMA), though instrument-specific design features significantly influence calibration characteristics. The segmented detector design in GF-5A AHSI, the temperature-dependent behavior of PRISMA's prism-based spectrometer, and the simplified calibration approach of EMIT each present unique calibration challenges that must be addressed in operational data processing.

Future developments should focus on incorporating more flexible spectral response function parameterizations beyond the Gaussian assumption, utilizing location- and time-specific atmospheric profiles from reanalysis datasets, and extending the approach to address systematic spectral response function asymmetries. The integration of updated spectroscopic databases and LBL radiative transfer calculations may further improve calibration accuracy, particularly in the SWIR region where fine-scale absorption structures are critical for accurate FWHM characterization.

The scene-based calibration algorithm developed here offers a practical complement to on-board hardware systems and provides full FOV spectral characterization that many hardware approaches cannot achieve. Regular spectral monitoring becomes essential as instruments age, particularly given the substantial degradation observed in PRISMA after six years of operation. With numerous hyperspectral missions planned for the next decade, consistent calibration methodologies will be critical for maintaining data quality and enabling meaningful comparisons across different instruments and time periods. The inter-instrument analysis presented here demonstrates how factors such as detector design, dispersive elements, and thermal management directly influence long-term spectral stability, providing valuable guidance for both current operations and future mission planning.

Acknowledgements

This study was funded by the National Natural Science Foundation of China (Grant No. 42475144), the National Key Research and Development Program of China (Grant No. 2022YFB3904801), the Hubei Provincial Natural Science Foundation (Grant Nos. 2023AFB834 and 202CFD015), the Beijing Natural Science Foundation (Grant No. L211045), and the Fundamental Research Funds for the Central Universities (Grant No. 4106-413000027). We gratefully acknowledge the Italian Space Agency (ASI) for providing PRISMA data, the German Aerospace Center (DLR) for providing EnMAP data, NASA for providing EMIT data, and the China Centre for Resources Satellite Data and Application (CRESDA) for providing GF-5A AHSI data. We appreciate the assistance of the libRadtran team, including Bernhard Mayer and Josef Gasteiger. This work also benefited from open-source software packages, including matplotlib and pandas.

References

Asadzadeh, S., Koellner, N., Chabrillat, S., 2024. Detecting rare earth elements using enmap hyperspectral satellite data: a case study from mountain pass, california. Scientific Reports 14, 20766.

Ayasse, A.K., Cusworth, D., O'Neill, K., Fisk, J., Thorpe, A.K., Duren, R., 2023. Performance and sensitivity of column-wise and pixel-wise methane retrievals for imaging spectrometers. Atmospheric Measurement Techniques 16, 6065–6074.

Ayasse, A.K., Dennison, P.E., Foote, M., Thorpe, A.K., Joshi, S., Green, R.O., Duren, R.M., Thompson, D.R., Roberts, D.A., 2019. Methane mapping with future satellite imaging spectrometers. Remote Sensing 11, 3054.

Baur, S., Mücke, M., Sang, B., Wachter, R., Lettner, M., Honold, H.P., Sornig, M., Fischer, S., 2023. Pre-flight calibration and characterization of the enmap sensor, in: International Conference on Space Optics—ICSO 2022, SPIE. pp. 2092–2112.

Baur, S., Wachter, R., Basili, P., Lettner, M., Mücke, M., Sornig, M., Fischer, S., 2019. Calibration and characterization of the enmap hyperspectral imager, in: Sensors, Systems, and Next-Generation Satellites XXIII, SPIE. pp. 265–272.

Borger, C., Beirle, S., Butz, A., Scheidweiler, L.O., Wagner, T., 2025. High-resolution observations of no2 and co2 emission plumes from enmap satellite measurements. Environmental Research Letters 20, 044034.

Bradley, E.S., Leifer, I., Roberts, D.A., Dennison, P.E., Washburn, L., 2011. Detection of marine methane emissions with aviris band ratios. Geophysical Research Letters 38.

Braga, F., Fabbretto, A., Vanhellemont, Q., Bresciani, M., Giardino, C., Scarpa, G.M., Manfè, G., Concha, J.A., Brando, V.E., 2022. Assessment of prisma water reflectance using autonomous hyperspectral radiometry. ISPRS Journal of Photogrammetry and Remote Sensing 192, 99–114. URL: `https://www.sciencedirect.com/science/article/pii/S0924271622002179`, doi:`https://doi.org/10.1016/j.isprsjprs.2022.08.009`.

Carmon, N., Thompson, D.R., Bohn, N., Susiluoto, J., Turmon, M., Brodrick, P.G., Connelly, D.S., Braverman, A., Cawse-Nicholson, K., Green, R.O., et al., 2020. Uncertainty quantification for a global imaging spectroscopy surface composition investigation. Remote Sensing of Environment 251, 112038.

Chabrillat, S., Foerster, S., Segl, K., Beamish, A., Brell, M., Asadzadeh, S., Milewski, R., Ward, K.J., Brosinsky, A., Koch, K., et al., 2024. The enmap spaceborne imaging spectroscopy mission: Initial scientific results two years after launch. Remote Sensing of Environment 315, 114379.

Chrien, T.G., Green, R.O., Eastwood, M.L., 1990. Accuracy of the spectral and radiometric laboratory calibration of the airborne visible/infrared imaging spectrometer, in: Imaging Spectroscopy of the Terrestrial Environment, SPIE. pp. 37–49.

Cogliati, S., Sarti, F., Chiarantini, L., Cosi, M., Lorusso, R., Lopinto, E., Miglietta, F., Genesio, L., Guanter, L., Damm, A., et al., 2021. The prisma imaging spectroscopy mission: overview and first performance analysis. Remote sensing of environment 262, 112499.

Coppo, P., Brandani, F., Faraci, M., Sarti, F., Dami, M., Chiarantini, L., Ponticelli, B., Giunti, L., Fossati, E., Cosi, M., 2020. Leonardo spaceborne infrared payloads for earth observation: Slstrs for copernicus sentinel 3 and prisma hyperspectral camera for prisma satellite. Applied Optics 59, 6888–6901.

Cosnefroy, H., Leroy, M., Briottet, X., 1996. Selection and characterization of saharan and arabian desert sites for the calibration of optical satellite sensors. Remote Sensing of Environment 58, 101–114.

Cusworth, D.H., Duren, R.M., Ayasse, A.K., Jiorle, R., Howell, K., Aubrey, A., Green, R.O., Eastwood, M.L., Chapman, J.W., Thorpe, A.K., et al., 2024. Quantifying methane emissions from united states landfills. Science 383, 1499–1504.

Cusworth, D.H., Thorpe, A.K., Miller, C.E., Ayasse, A.K., Jiorle, R., Duren, R.M., Nassar, R., Mastrogiacomo, J.P., Nelson, R.R., 2023. Two years of satellite-based carbon dioxide emission quantification at the world's largest coal-fired power plants. Atmospheric Chemistry and Physics 23, 14577–14591.

Duren, R.M., Thorpe, A.K., Foster, K.T., Rafiq, T., Hopkins, F.M., Yadav, V., Bue, B.D., Thompson, D.R., Conley, S., Colombi, N.K., et al., 2019. California's methane super-emitters. Nature 575, 180–184.

Emde, C., Buras-Schnell, R., Kylling, A., Mayer, B., Gasteiger, J., Hamann, U., Kylling, J., Richter, B., Pause, C., Dowling, T., et al., 2016. The libradtran software package for radiative transfer calculations (version 2.0. 1). Geoscientific Model Development 9, 1647–1672.

EnMAP, 2024. Swir dark signal effect corrected. URL: `https://www.enmap.org/news/2024-11-19/`.

Folkman, M.A., Pearlman, J., Liao, L.B., Jarecke, P.J., 2001. Eo-1/hyperion hyperspectral imager design, development, characterization, and calibration. Hyperspectral Remote Sensing of the Land and Atmosphere 4151, 40–51.

Foote, M.D., Dennison, P.E., Sullivan, P.R., O'Neill, K.B., Thorpe, A.K., Thompson, D.R., Cusworth, D.H., Duren, R., Joshi, S.C., 2021. Impact of scene-specific enhancement spectra on matched filter greenhouse gas retrievals from imaging spectroscopy. Remote Sensing of Environment 264, 112574.

Foote, M.D., Dennison, P.E., Thorpe, A.K., Thompson, D.R., Jongaramrungruang, S., Frankenberg, C., Joshi, S.C., 2020. Fast and accurate retrieval of methane concentration from imaging spectrometer data using sparsity prior. IEEE Transactions on Geoscience and Remote Sensing 58, 6480–6492.

Frankenberg, C., Platt, U., Wagner, T., 2005. Iterative maximum a posteriori (imap)-doas for retrieval of strongly absorbing trace gases: Model studies for ch 4 and co 2 retrieval from near infrared spectra of sciamachy onboard envisat. Atmospheric Chemistry and Physics 5, 9–22.

Gao, B.C., Heidebrecht, K.B., Goetz, A.F., 1993. Derivation of scaled surface reflectances from aviris data. Remote sensing of Environment 44, 165–178.

Gao, B.C., Kaufman, Y.J., 2003. Water vapor retrievals using moderate resolution imaging spectroradiometer (modis) near-infrared channels. Journal of Geophysical Research: Atmospheres 108.

Gao, B.C., Montes, M.J., Davis, C.O., 2004. Refinement of wavelength calibrations of hyperspectral imaging data using a spectrum-matching technique. Remote Sensing of Environment 90, 424–433.

Gasteiger, J., Emde, C., Mayer, B., Buras, R., Buehler, S., Lemke, O., 2014. Representative wavelengths absorption parameterization applied to satellite channels and spectral bands. Journal of Quantitative Spectroscopy and Radiative Transfer 148, 99–115.

Goetz, A.F., 2009. Three decades of hyperspectral remote sensing of the earth: A personal view. Remote sensing of environment 113, S5–S16.

Goetz, A.F., Vane, G., Solomon, J.E., Rock, B.N., 1985. Imaging spectrometry for earth remote sensing. science 228, 1147–1153.

Green, R.O., Eastwood, M.L., Sarture, C.M., Chrien, T.G., Aronsson, M., Chippendale, B.J., Faust, J.A., Pavri, B.E., Chovit, C.J., Solis, M., et al., 1998. Imaging spectroscopy and the airborne visible/infrared imaging spectrometer (aviris). Remote sensing of environment 65, 227–248.

Green, R.O., Mahowald, N., Ung, C., , D.R., Bator, L., Bennet, M., Bernas, M., Blackway, N., Bradley, C., Cha, J., et al., 2020. The earth surface mineral dust source investigation: An earth science imaging spectroscopy mission, in: 2020 IEEE aerospace conference, IEEE. pp. 1–15.

Green, R.O., Schaepman, M.E., Mouroulis, P., Geier, S., Shaw, L., Hueini, A., Bernas, M., McKinley, I., Smith, C., Wehbe, R., et al., 2022. Airborne visible/infrared imaging spectrometer 3 (aviris-3), in: 2022 IEEE Aerospace Conference (AERO), IEEE. pp. 1–10.

Guanter, L., Estellés, V., Moreno, J., 2007. Spectral calibration and atmospheric correction of ultra-fine spectral and spatial resolution remote sensing data. application to casi-1500 data. Remote Sensing of Environment 109, 54–65.

Guanter, L., Irakulis-Loitxate, I., Gorroño, J., Sánchez-García, E., Cusworth, D.H., Varon, D.J., Cogliati, S., Colombo, R., 2021. Mapping methane point emissions with the prisma spaceborne imaging spectrometer. Remote Sensing of Environment 265, 112671.

Guanter, L., Kaufmann, H., Segl, K., Foerster, S., Rogass, C., Chabrillat, S., Kuester, T., Hollstein, A., Rossner, G., Chlebek, C., et al., 2015. The enmap spaceborne imaging spectroscopy mission for earth observation. Remote Sensing 7, 8830–8857.

Guanter, L., Richter, R., Kaufmann, H., 2009a. On the application of the modtran4 atmospheric radiative transfer code to optical remote sensing. International Journal of Remote Sensing 30, 1407–1424.

Guanter, L., Richter, R., Moreno, J., 2006. Spectral calibration of hyperspectral imagery using atmospheric absorption features. Applied optics 45, 2360–2370.

Guanter, L., Roger, J., Sharma, S., Valverde, A., Irakulis-Loitxate, I., Gorroño, J., Zhang, X., Schuit, B.J., Maasakkers, J.D., Aben, I., et al., 2024. Multisatellite data depicts a record-breaking methane leak from a well blowout. Environmental Science & Technology Letters 11, 825–830.

Guanter, L., Segl, K., Sang, B., Alonso, L., Kaufmann, H., Moreno, J., 2009b. Scene-based spectral calibration assessment of high spectral resolution imaging spectrometers. Optics express 17, 11594–11606.

Han, G., Pei, Z., Shi, T., Mao, H., Li, S., Mao, F., Ma, X., Zhang, X., Gong, W., 2024. Unveiling unprecedented methane hotspots in china's leading coal production hub: A satellite mapping revelation. Geophysical Research Letters 51, e2024GL109065.

Hersbach, H., Bell, B., Berrisford, P., Hirahara, S., Horányi, A., Muñoz-Sabater, J., Nicolas, J., Peubey, C., Radu, R., Schepers, D., et al., 2020. The era5 global reanalysis. Quarterly journal of the royal meteorological society 146, 1999–2049.

Irakulis-Loitxate, I., Guanter, L., Liu, Y.N., Varon, D.J., Maasakkers, J.D., Zhang, Y., Chulakadabba, A., Wofsy, S.C., Thorpe, A.K., Duren, R.M., et al., 2021. Satellite-based survey of extreme methane emissions in the permian basin. Science Advances 7, eabf4507.

Jacob, D.J., Varon, D.J., Cusworth, D.H., Dennison, P.E., Frankenberg, C., Gautam, R., Guanter, L., Kelley, J., McKeever, J., Ott, L.E., et al., 2022. Quantifying methane emissions from the global scale down to point sources using satellite observations of atmospheric methane. Atmospheric Chemistry and Physics Discussions 2022, 1–44.

Jaworske, D.A., 1999. Changes in the optical properties of materials are observed after 18 months in low earth orbit. Research and Technology 1998 .

Kokaly, R.F., Asner, G.P., Ollinger, S.V., Martin, M.E., Wessman, C.A., 2009. Characterizing canopy biochemistry from imaging spectroscopy and its application to ecosystem studies. Remote sensing of environment 113, S78–S91.

Kuhlmann, G., Hueni, A., Damm, A., Brunner, D., 2016. An algorithm for in-flight spectral calibration of imaging spectrometers. Remote Sensing 8, 1017.

Kukkurainen, A., Mikkonen, A., Arola, A., Lipponen, A., Kolehmainen, V., Sabater, N., 2025. Hapi2libis (v1. 0): A new tool for flexible high resolution radiative transfer computations with libradtran (version 2.0. 5). EGUsphere 2025, 1–20.

Labate, D., Ceccherini, M., Cisbani, A., De Cosmo, V., Galeazzi, C., Giunti, L., Melozzi, M., Pieraccini, S., Stagi, M., 2009. The prisma payload optomechanical design, a high performance instrument for a new hyperspectral mission. Acta Astronautica 65, 1429–1436. URL: https://www.sciencedirect.com/science/article/pii/S0094576509002173, doi:https://doi.org/10.1016/j.actaastro.2009.03.077.

Li, F., Bai, S., Lin, K., Feng, C., Sun, S., Zhao, S., Wang, Z., Zhou, W., Zhou, C., Zhang, Y., 2024. Satellite-based surveys reveal substantial methane point-source emissions in major oil & gas basins of north america during 2022–2023. Journal of Geophysical Research: Atmospheres 129, e2024JD040870.

Mouroulis, P., Green, R.O., Chrien, T.G., 2000. Design of pushbroom imaging spectrometers for optimum recovery of spectroscopic and spatial information. Applied Optics 39, 2210–2220.

Nelder, J.A., Mead, R., 1965. A simplex method for function minimization. The computer journal 7, 308–313.

Niu, C., Tan, K., Wang, X., Han, B., Ge, S., Du, P., Wang, F., 2021. Radiometric cross-calibration of the zy1-02d hyperspectral imager using the gf-5 ahsi imager. IEEE Transactions on Geoscience and Remote Sensing 60, 1–12.

Pahlevan, N., Schott, J.R., 2013. Leveraging eo-1 to evaluate capability of new generation of landsat sensors for coastal/inland water studies. IEEE Journal of selected topics in applied earth observations and remote sensing 6, 360–374.

Pei, Z., Han, G., Mao, H., Chen, C., Shi, T., Yang, K., Ma, X., Gong, W., 2023. Improving quantification of methane point source emissions from imaging spectroscopy. Remote Sensing of Environment 295, 113652.

Pellegrino, A., Fabbretto, A., Bresciani, M., de Lima, T.M.A., Braga, F., Pahlevan, N., Brando, V.E., Kratzer, S., Gianinetto, M., Giardino, C., 2023. Assessing the accuracy of prisma standard reflectance products in globally distributed aquatic sites. Remote Sensing 15, 2163.

Press, W.H., Teukolsky, S.A., Vetterling, W.T., Flannery, B.P., 2007. Numerical recipes: the art of scientific computing. 3rd ed., Cambridge University Press, Cambridge.

Roberts, D.A., Bradley, E.S., Cheung, R., Leifer, I., Dennison, P.E., Margolis, J.S., 2010. Mapping methane emissions from a marine geological seep source using imaging spectrometry. Remote Sensing of Environment 114, 592–606.

Roger, J., Irakulis-Loitxate, I., Valverde, A., Gorroño, J., Chabrillat, S., Brell, M., Guanter, L., 2024. High-resolution methane mapping with the enmap satellite imaging spectroscopy mission. IEEE Transactions on Geoscience and Remote Sensing .

Storch, T., Honold, H.P., Chabrillat, S., Habermeyer, M., Tucker, P., Brell, M., Ohndorf, A., Wirth, K., Betz, M., Kuchler, M., et al., 2023. The enmap imaging spectroscopy mission towards operations. Remote Sensing of Environment 294, 113632.

Tansock, J., Bancroft, D., Butler, J., Cao, C., Datla, R., Hansen, S., Helder, D., Kacker, R., Latvakoski, H., Mylnczak, M., et al., 2015. Guidelines for radiometric calibration of electro-optical instruments for remote sensing .

Thompson, D., Leifer, I., Bovensmann, H., Eastwood, M., Fladeland, M., Frankenberg, C., Gerilowski, K., Green, R., Kratwurst, S., Krings, T., et al., 2015. Real-time remote detection and measurement for airborne imaging spectroscopy: a case study with methane. Atmospheric Measurement Techniques 8, 4383–4397.

Thompson, D., Thorpe, A., Frankenberg, C., Green, R., Duren, R., Guanter, L., Hollstein, A., Middleton, E., Ong, L., Ungar, S., 2016. Space-based remote imaging spectroscopy of the aliso canyon ch4 superemitter. Geophysical Research Letters 43, 6571–6578.

Thompson, D.R., Boardman, J.W., Eastwood, M.L., Green, R.O., Haag, J.M., Mouroulis, P., Van Gorp, B., 2018a. Imaging spectrometer stray spectral response: In-flight characterization, correction, and validation. Remote Sensing of Environment 204, 850–860.

Thompson, D.R., Green, R.O., Bradley, C., Brodrick, P.G., Mahowald, N., Dor, E.B., Bennett, M., Bernas, M., Carmon, N., Chadwick, K.D., et al., 2024. On-orbit calibration and performance of the emit imaging spectrometer. Remote Sensing of Environment 303, 113986. URL: https://www.sciencedirect.com/science/article/pii/S0034425723005382.

Thompson, D.R., Natraj, V., Green, R.O., Helmlinger, M.C., Gao, B.C., Eastwood, M.L., 2018b. Optimal estimation for imaging spectrometer atmospheric correction. Remote sensing of environment 216, 355–373.

Thorpe, A.K., Frankenberg, C., Aubrey, A., Roberts, D., Nottrott, A., Rahn, T., Sauer, J., Dubey, M., Costigan, K., Arata, C., et al., 2016. Mapping methane concentrations from a controlled release experiment using the next generation airborne visible/infrared imaging spectrometer (aviris-ng). Remote Sensing of Environment 179, 104–115.

Thorpe, A.K., Green, R.O., Thompson, D.R., Brodrick, P.G., Chapman, J.W., Elder, C.D., Irakulis-Loitxate, I., Cusworth, D.H., Ayasse, A.K., Duren, R.M., et al., 2023. Attribution of individual methane and carbon dioxide emission sources using emit observations from space. Science advances 9, eadh2391.

Yamamoto, S., Tsuchida, S., Urai, M., Mizuochi, H., Iwao, K., Iwasaki, A., 2022. Initial analysis of spectral smile calibration of hyperspectral imager suite (hisui) using atmospheric absorption bands. IEEE Transactions on Geoscience and Remote Sensing 60, 1–15.

Yinnian, L., Dexin, S., Kaiqin, C., Shufeng, L., Mengyang, C., Juan, Y., et al., 2020a. Evaluation of gf-5 ahsi on-orbit instrument radiometric performance. National Remote Sensing Bulletin 24, 352–359.

Yinnian, L., Dexin, S., Xiaoning, H., Shufeng, L., Kaiqin, C., Mengyang, C., Qingjun, L., Zhiqiang, Z., Zhenyi, H., Weibo, D., et al., 2020b. Development of visible and short-wave infrared hyperspectral imager onboard gf-5 satellite. National Remote Sensing Bulletin 24, 333–344.

Supplementary Materials for

Scene-based spectral characterization of spaceborne imaging spectrometers in different spectral windows

Zhipeng Pei, Ge Han, Javier Roger, Wei Gong, Luis Guanter

*Corresponding author. Email: udhan@whu.edu.cn (Ge Han)

This PDF file includes:

Text S1
Tables S1
Figs. S1 to S12

Text S1. Effect of Instrument Spectral Convolution on Retrieved Surface Reflectance

The convolution of a product of two spectra does not mathematically equal the product of their individual convolutions, except when the instrument response function is infinitesimally narrow or or at least one of the spectra is not affected by the convolution. In other words, high-resolution radiance spectra simulated under surface albedo of 0.3 can derive surface reflectance of 0.3 for all channels through Eq.(2). However, convolved radiance spectra cannot yield the same result, as shown in Fig. S1. The convolved surface reflectance deviates from 0.3 in spectral regions where gaseous absorption is present, which may lead to slight issues in calibration algorithm.

Table S1. List of instrument abbreviations and definitions

Abbreviation	**Definition**
AVIRIS	Airborne Visible/Infrared Imaging Spectrometer
AHSI	Advanced Hyperspectral Imager
EMIT	Earth surface Mineral dust source InvesTigation
EnMAP	Environmental Mapping and Analysis Program
EO-1	Earth Observing-1
HISUI	Hyperspectral Imager Suite
PRISMA	PRecursore IperSpettrale della Missione Applicativa

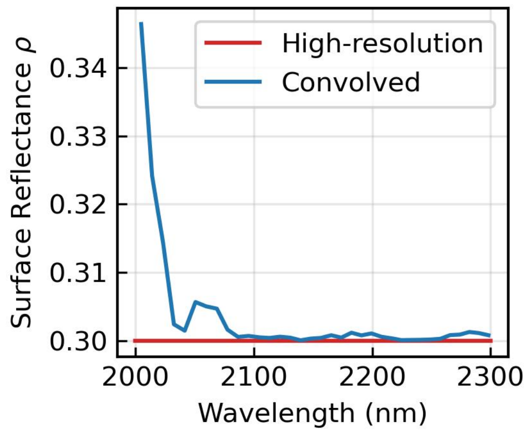

Fig. S1. Surface reflectance derived from simulated TOA radiance spectra. The red line represents results obtained from 0.1 nm high-resolution radiance spectra simulated by libRadtran, while the blue line represents results obtained from radiance spectra convolved with Gaussian SRF using EnMAP satellite spectral parameter. The input surface reflectance is 0.3.

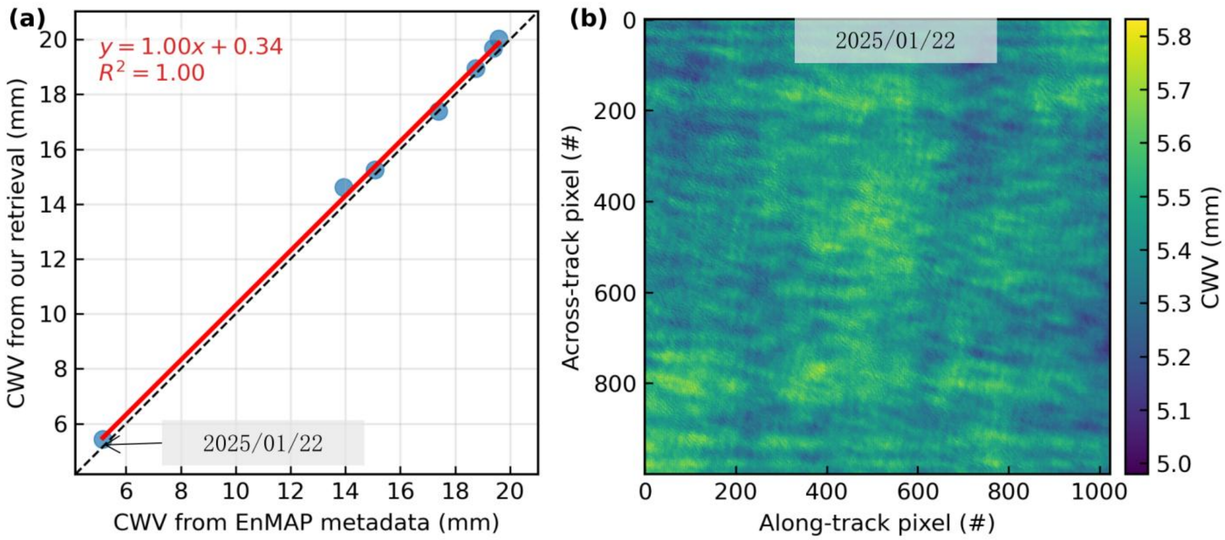

Fig. S2. Columnar water vaper (CWV) in EnMAP observation scenes. (a) CWV from our retrieval based on three-channel band ratioing technique v.s. those from EnMAP metadata. (b) The spatial distribution of CWV retrieved from EnMAP data collected on January 22, 2025.

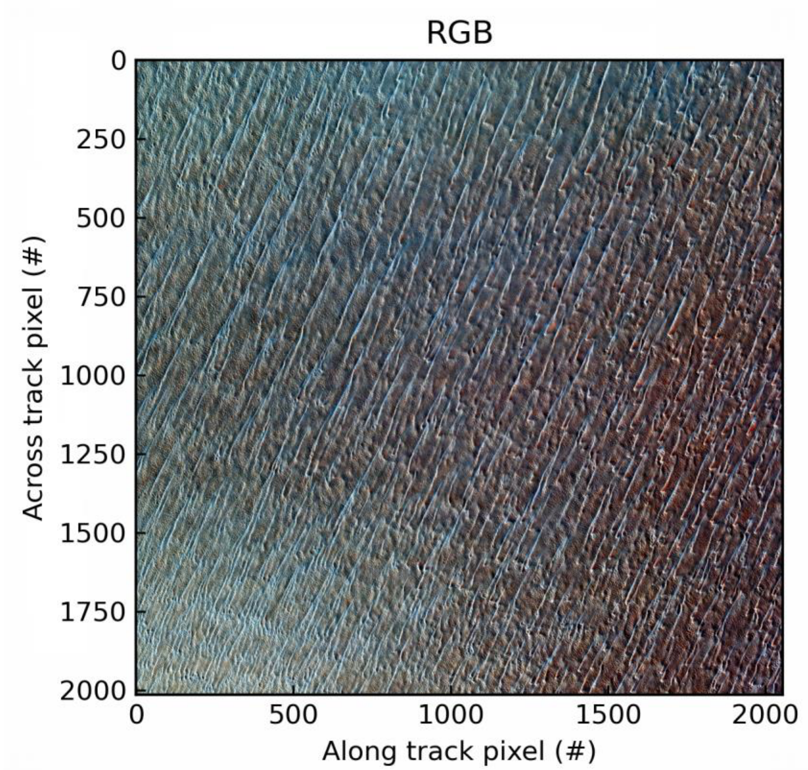

Fig. S3. Topographic variations at 30 m spatial resolution over homogeneous desert surface s. Data source: GF-5A AHSI (Scene ID: E50.5_N19.9_20241222_010851_L10000207894).

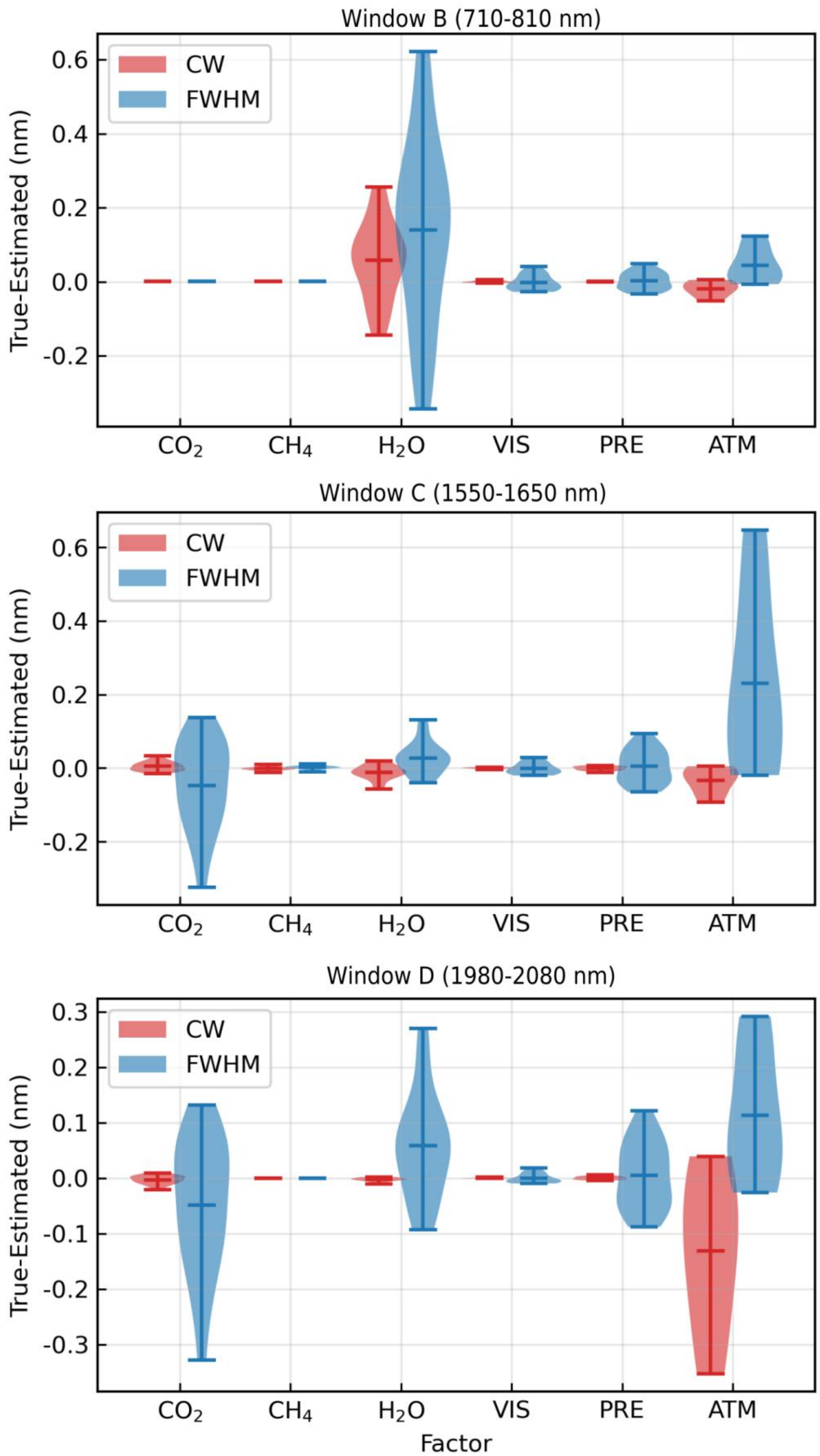

Fig. S4. Impact of different factors individually on the spectral calibration algorithm. The true CW and FWHM shifts are both 2 nm relative to EnMAP's nominal spectral configuration. The settings and abbreviations of each factor are shown in Table 2.

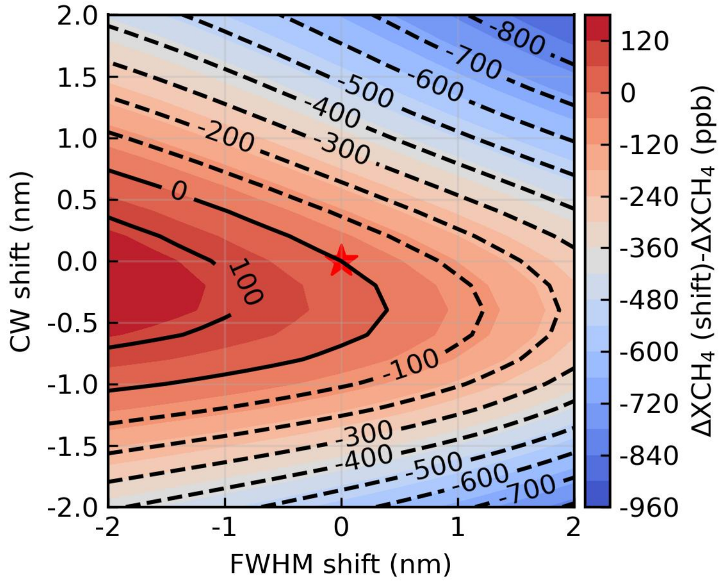

Fig. S5. ΔXCH_4 retrieval error as a function of spectral shift and channel broadening. The reference case (no shift) is marked with a red star. This analysis is based on EnMAP plume-containing imagery. The retrieved ΔXCH_4 using unshifted wavelength parameters is 1531 ppb. Data source: EnMAP (Scene ID: 20230923T081549Z_002_V010502)

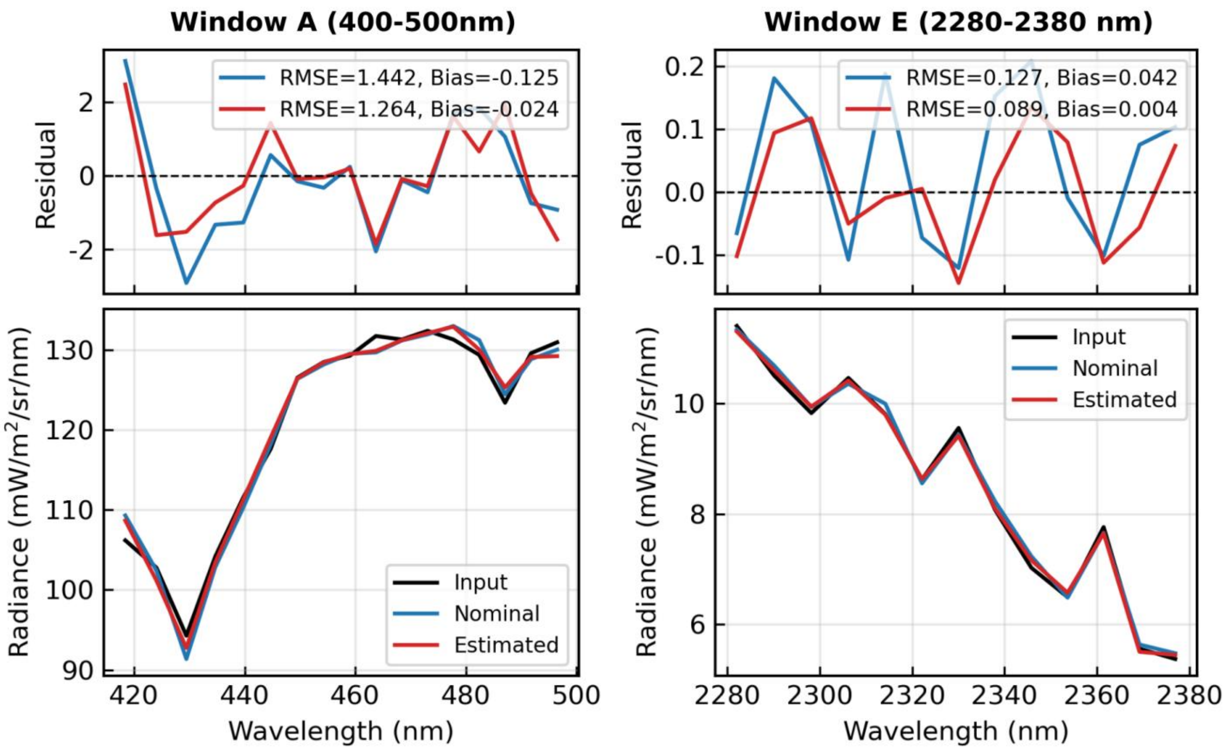

Fig. S6. Spectral fitting results for Window A (400-500 nm, left) and Window E (2280-2380 nm, right). Bottom panels show the comparison between the averaged observed spectrum (black) and modeled spectra calculated using nominal (blue) and algorithm-estimated (red) spectral configurations. Top panels display the corresponding fitting residuals, with root mean square error (RMSE) and bias values indicated. The improved fit achieved with the updated spectral parameters is evident from the reduced residuals and lower RMSE values compared to the nominal configuration. Data source: EnMAP (Scene ID: 20240702T103609Z_003_V010502).

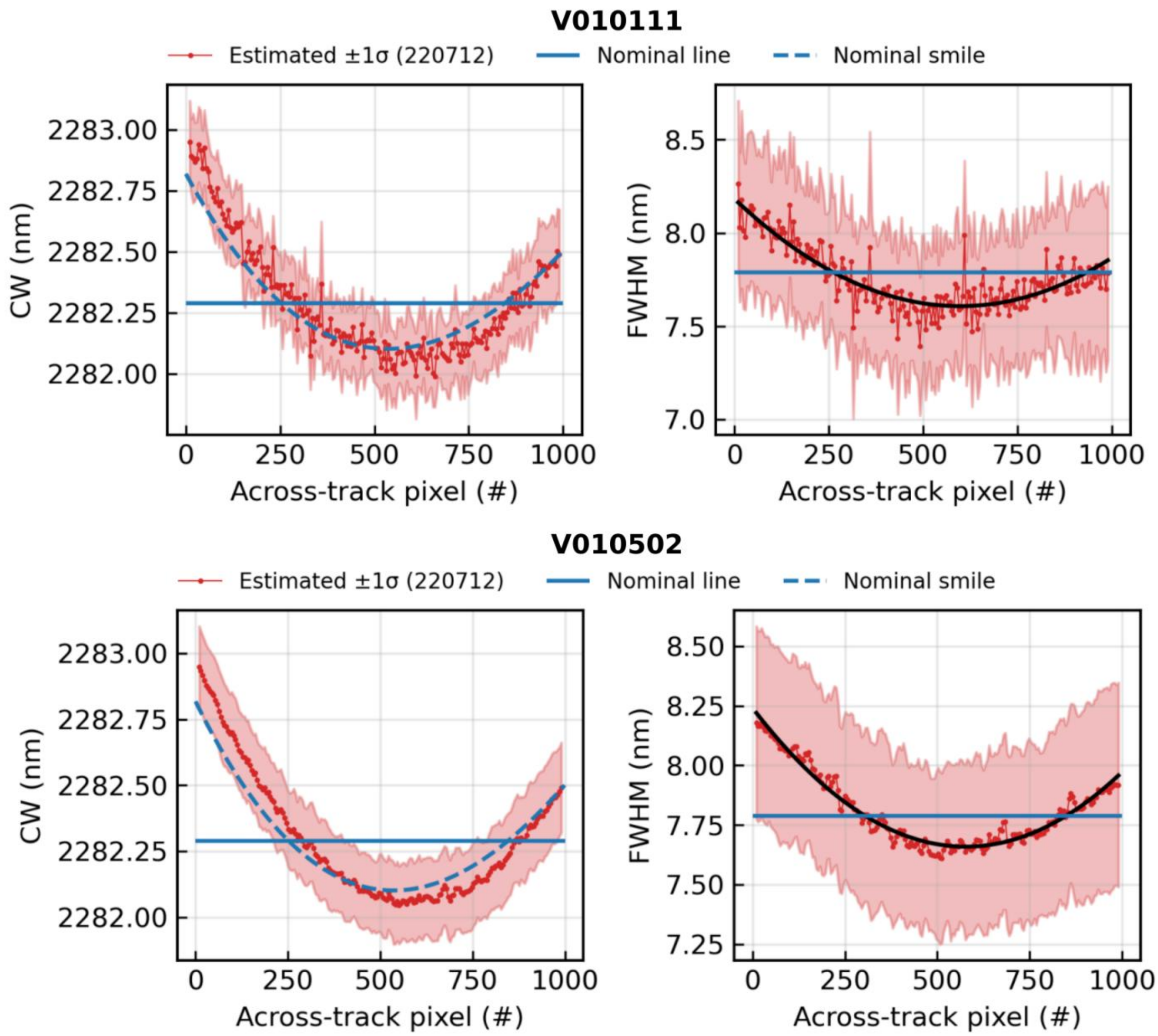

Fig. S7. Comparison of spectral calibration results using different EnMAP data processing versions for the same observation (20220712T104302Z_001). Top row shows results from version V010111, bottom row from version V010502. Left panels display center wavelength (CW) variations, right panels show full width at half maximum (FWHM) variations across the instrument swath. Red lines with shaded uncertainty bands represent algorithm-estimated values, blue solid lines show nominal mean values, and blue dashed lines indicate nominal smile patterns. The calibration results from the newer processing version (V010502) exhibit smoother across-track variations, demonstrating the impact of data processing improvements on spectral calibration accuracy.

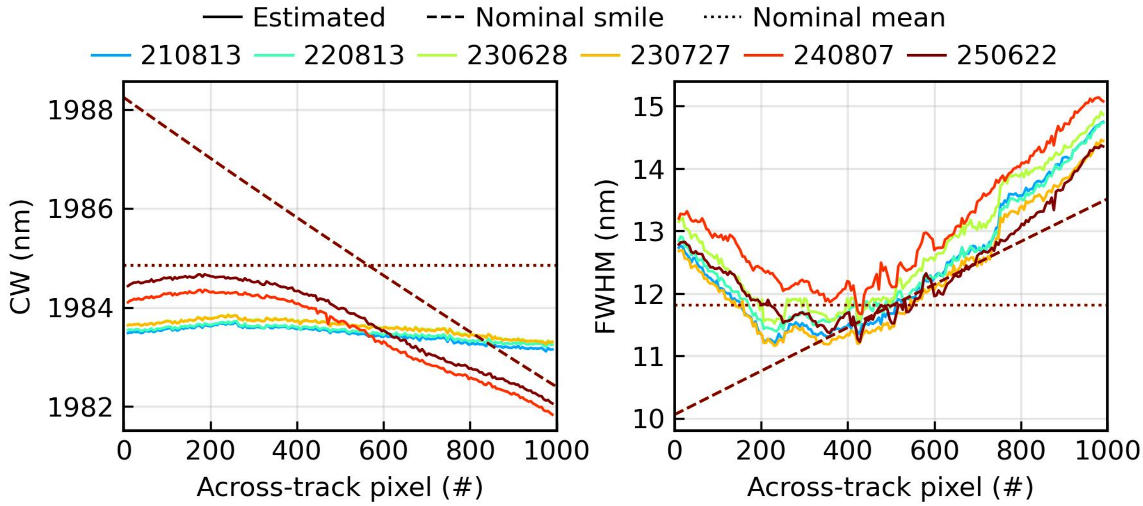

Fig. S8. Estimated and nominal PRISMA spectral parameters in the across-track direction for Window D at selected channels. The solid lines represent the values estimated by the scene-based spectral calibration algorithm, the dashed lines represent the nominal smile, and the dotted lines represent the nominal mean. Colors denote different observation dates. 200 across-track sample pixels were used for calibration to reduce computation time. The degradation in the SWIR is evident in window D.

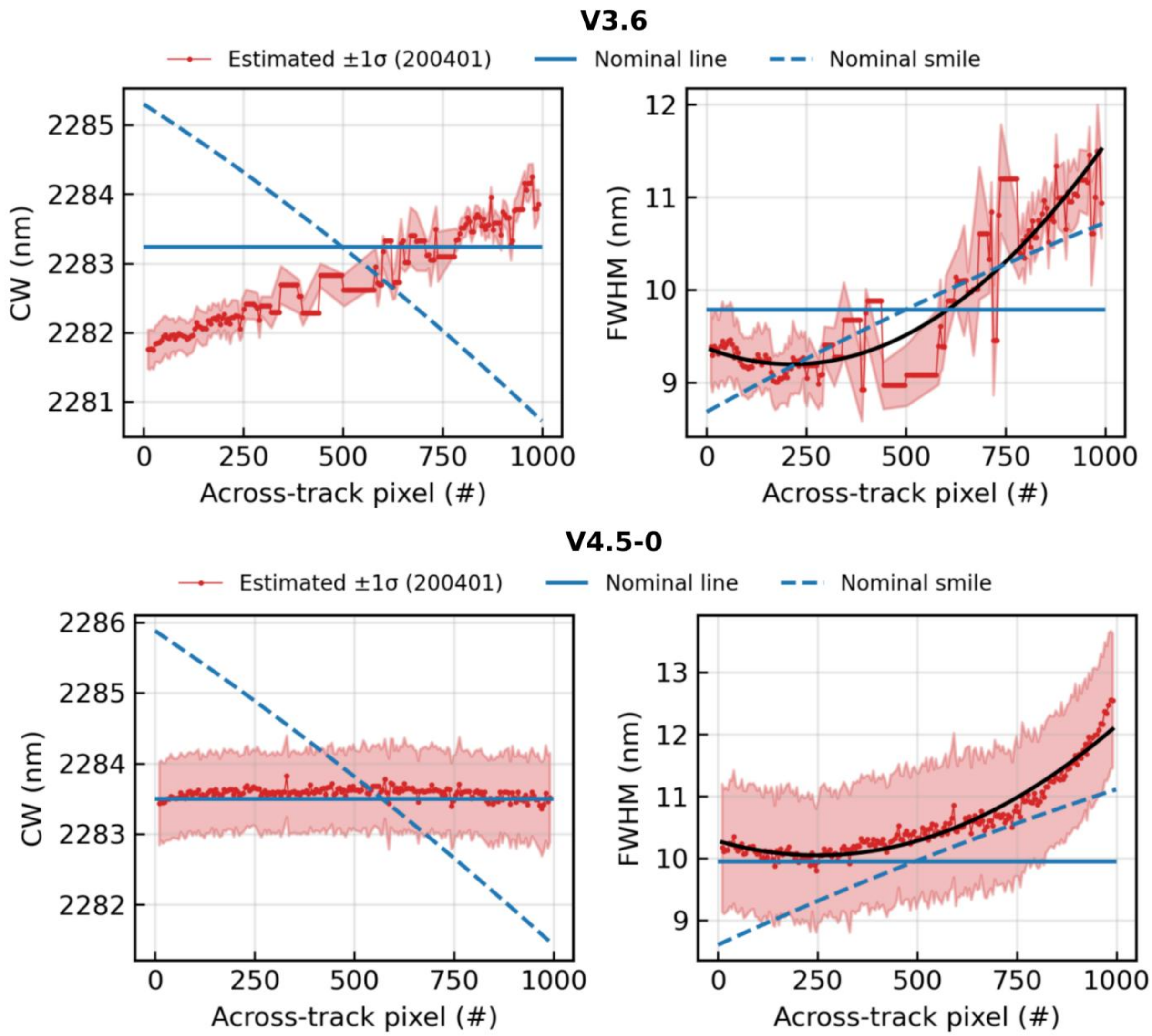

Fig. S9. Comparison of spectral calibration results using different PRISMAdata processing versions for the same observation (20200401085313_20200401085318_0001). Top row shows results from version V3.6, bottom row from version V4.5-0. Left panels display center wavelength (CW) variations, right panels show full width at half maximum (FWHM) variations across the instrument swath. Red lines with shaded uncertainty bands represent algorithm-estimated values, blue solid lines show nominal mean values, and blue dashed lines indicate nominal smile patterns. The calibration results from the newer processing version (V4.5-0) exhibit smoother across-track variations, demonstrating the impact of data processing improvements on spectral calibration accuracy.

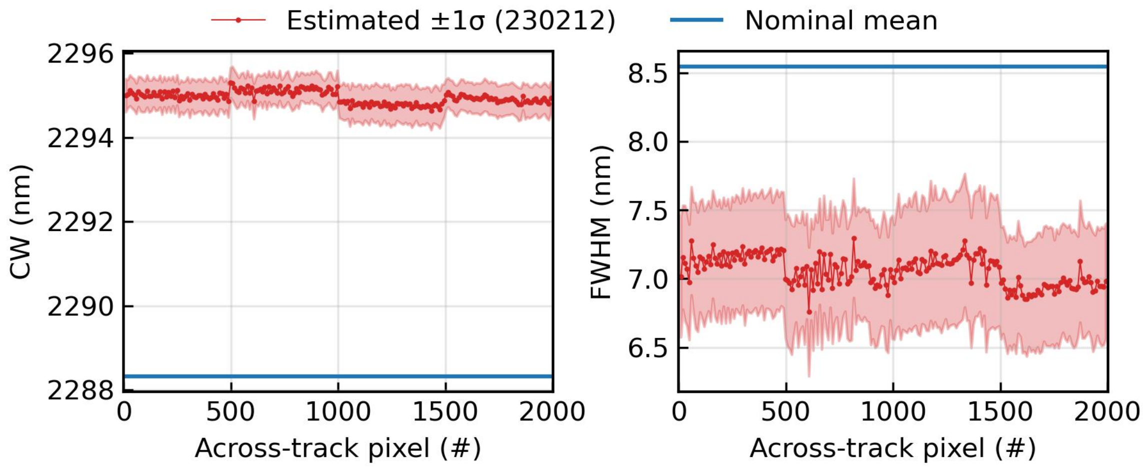

Fig. S10. Estimated and nominal GF-5A AHSI spectral parameters (CW and FWHM) in the across-track direction for Window E at selected channels. The red lines represent the spectral configuration estimated by the scene-based spectral calibration algorithm, the blue lines represent the nominal lines. Since the nominal spectral parameters still represent laboratory-based spectral characterization, there exists a CW difference of more than 6 nm between these parameters and the algorithm-estimated values.

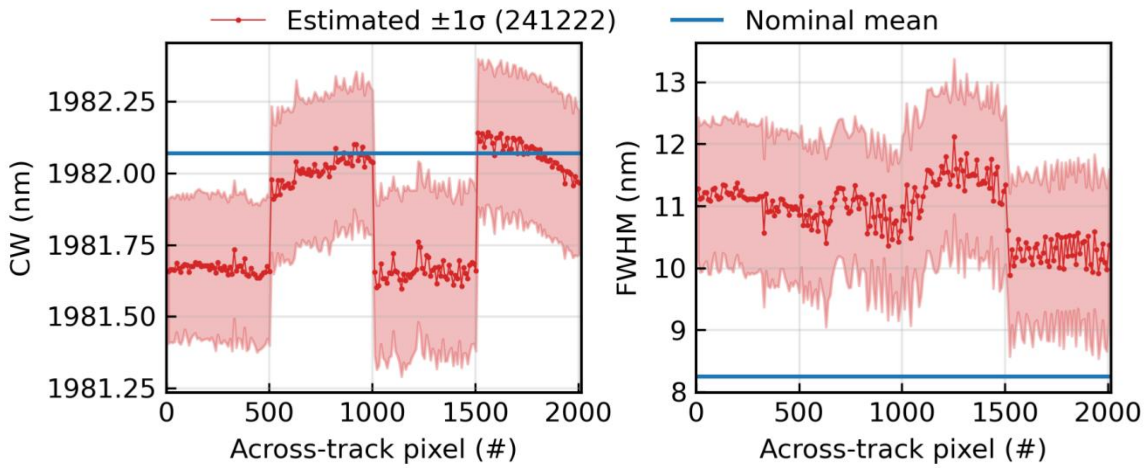

Fig. S11. Estimated and nominal GF-5A AHSI spectral parameters (CW and FWHM) in the across-track direction for Window D at selected channels. The solid lines represent the spectral configuration estimated by the scene-based spectral calibration algorithm, the dashed lines represent the nominal smile, and the dotted lines represent the nominal lines. The phenomenon of segmented variations is also observed in Window D.

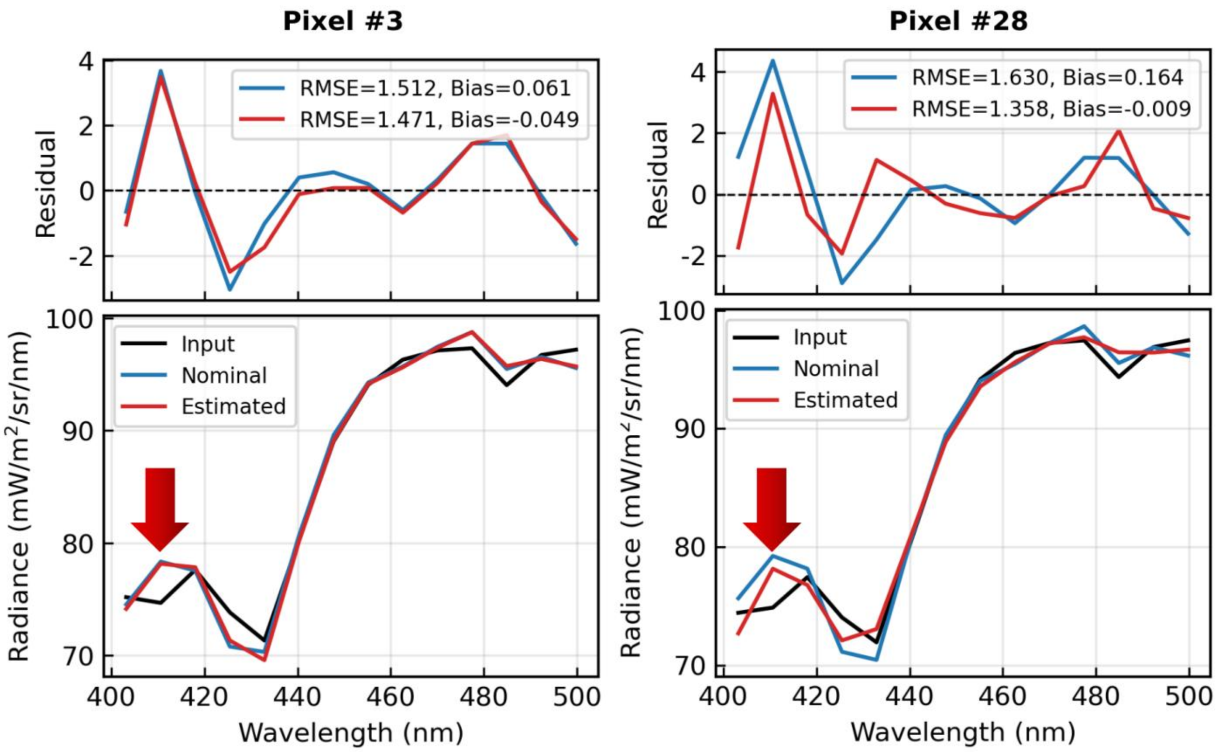

Fig. S12. Spectral fitting results for two representative across-track pixels: pixel #3 (left) and pixel #28 (right) in Window A. Bottom panels show the comparison between the averaged observed spectrum (black) and modeled spectra calculated using nominal (blue) and algorithm-estimated (red) spectral configurations. Top panels display the corresponding fitting residuals with root mean square error (RMSE) and bias values. Red arrows highlight the 400-420 nm spectral range where poor fitting occurs across all pixels due to instrument artifacts or calibration issues in the blue region. The improved spectral fitting achieved with the updated parameters is evident from the reduced residuals, though challenges remain in the shortest wavelength bands for both pixels shown. Consequently, we excluded these bands and adopted the 420-500 nm range for EMIT's Window A. Data source: EMIT (Scene ID: 20230724T135724_2320509_028).